Spring 5-1-2005

Studies on Novel Semiconductor Detectors and Front-End Electronics for Heavy Flavor Decay Studies

Gustavo Kertzscher

1. INTRODUCTION

Elementary particle physicists study the structure of matter by delving into nature at the smallest scales possible. During the 1950s, accelerator physics started to take a considerable role in the field of elementary particle physics. With particle accelerators, physicists managed to collide particles at such high energy concentrations that new particles were produced, according to Einstein's relation between relativistic energy and rest mass, $E=mc^2$ (Fermilab). As physicists learned how to collide particles at higher and higher energies, many new discoveries of particles and their properties accumulated and formed a new theory called the Standard Model of particles and interactions (SM). The SM is a combination of three of the four known fundamental forces: electromagnetism, strong nuclear force, and weak nuclear force (gravity is excluded), and also relates these forces with known fundamental particles (quarks and leptons) (BTeV).

Demands for proper observations of particle collisions at higher energies have resulted in modern particle accelerators of enormous dimensions. Current High Energy Physics (HEP) detectors have become the size of apartment houses and are prepared to observe a million particle collision events each second. A proper design is crucial in order to save the most interesting events for experimental analysis, and technology advancement has naturally taken a crucial role in the advancement of HEP. One HEP detector may be developed by hundreds of physicists from different fields in physics, and may take up to fifteen years to develop.

The Syracuse University HEP group is generally focused on uncovering answers beyond the reach of the SM. One feature in the SM relates the mass eigenstates of the Hamiltonian with the flavor eigenstates of the Weak Interaction, and allows for the phenomenon known as CP-violation (Blusk). CP violation is an essential element to explain the matter-dominated universe that we see nowadays. It has been seen in K^0-K^0bar oscillations (Cronin, 1964), and most recently in B^0-B^0bar oscillations in the experiments BaBar and Belle. The measured CP violation unfortunately does not explain the matter-antimatter asymmetry and thus new information is needed. The decays of beauty-flavored hadrons (exotic subatomic particles that contain the beauty quark) are an ideal means to search for new CP phases (BTeV). In order to hunt for these phases, the SU HEP group participated in the design of the BTeV detector, now terminated as a result of the President's budget. The work described in this thesis was part of the research and development towards this detector. The BTeV experiment was expected to run in 2009 at the Fermilab Tevatron, which is a particle accelerator capable of accelerating protons and antiprotons to energies of the order of TeV, which is a suitable energy for observing CP-violation in the b-quark sector (Blusk).

My Honors Thesis Project (HTP) presents sensor characterizations for two different BTeV detector components. In the first part, I verified static properties of different silicon micropattern detectors. These detectors are key elements in most modern experimental particle physics experiments. The advances in precision photolithography allow forming micropatterns that

make very precise position measurements possible. In particle physics applications, this property is used to make precise measurements of the trajectories of the charged tracks produced in high energy collisions. The spatial resolution is an asset that is exploited in other areas of science and technology, such as biology and diagnostic medicine. The pixel detector system that was developed for the BTeV experiment was an example of a state-of-the-art application of this technology. Other measurements that I performed were undertaken in the context of the RD50 collaboration, based at CERN, in Geneva, Switzerland, including several US Institutions.

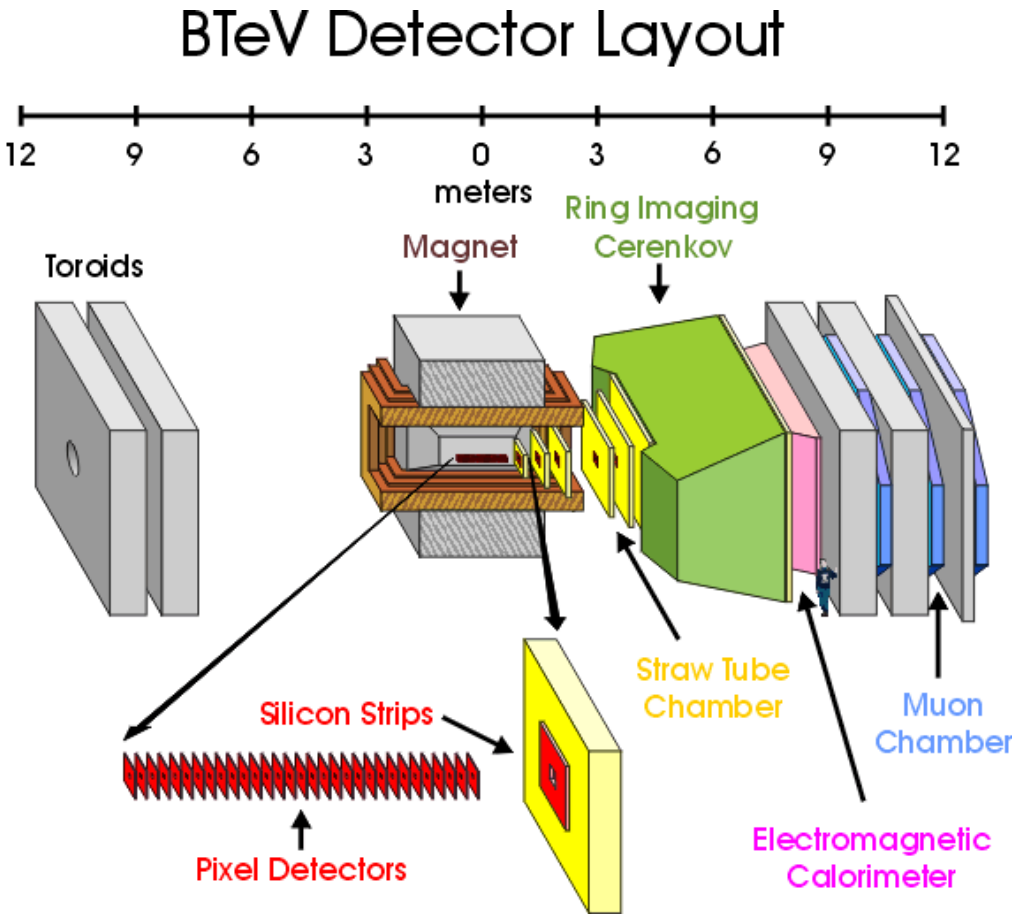

Figure 1: This figure represents the different parts of the BTeV detector. The studies I made were related to the Pixel Detectors and the Ring Imaging Cherenkov detector. Figure copied from (BTeV).

In the second part of my HTP, I studied dynamic properties of front-end electronics for the BTeV Ring Imaging Cherenkov detector (BTeV RICH) – a part of the BTeV detector that is crucial for particle identification, and has the sensors chosen for this system, called Multi Anode Photo Multiplier Tubes (MaPMT), attached to it. The BTeV RICH measures photon emissions due to a phenomenon called Cherenkov radiation, that is caused when charged particles' travel in a medium with greater speed than light's speed in that same medium (Leo, 1994). The RICH detected angle of the emitted photons, with respect to the charged particle's trajectory, and the silicon detector verified particle momentum, identify the particle (Blusk). A central role in RICH detector front-end electronics is that of the Application-Specified Integrated Circuit (ASIC), since it digitizes the MaPMT signals to make data acquisition possible. Studies of the front-end electronic dynamic properties are necessary to understand limitations in the readout. The measurements I made were the first of its kind to help better understand these novel devices.

2. SILICON DETECTOR MEASUREMENTS

In high energy physics experiments, the first step in the detector production is the fabrication of silicon wafers that contain the detectors and some test structures allowing for key process properties to be measured. The first step in the qualification of these detectors is the measurement of their static properties (current versus reverse bias and capacitance versus reverse bias) to verify that the detectors have the desired properties that were predicted from electrostatic simulations.

I characterized a full wafer for a BTeV prototype detector and studied some RD50 silicon detector prototype structures. The SU HEP group contributed to the RD50 collaboration with static property simulations for the quasi-3D structure, and my measurements served as the first set of experimental characterizations for these structures. This kind of investigation takes an integral part for preparations of current particle physics experiments. Static measurements are intended to ensure physicists that the devices are ready to make an optimal response to dynamic conditions, for instance when a particle crosses the detector.

The laboratory facility described in this chapter was developed in concomitance with these measurements, and I helped in developing measurement procedures to perform characterizations in a precise manner.

2.a DESCRIPTION OF SILICON DETECTORS

Inner tracking systems in modern HEP detectors demand a high resolution due to the close space between the initial scattered particles (BTeV). Advancements in photolithography have resulted in micropattern silicon detectors that meet these demands. The Tesla and quasi-3D structures present different geometric doping configurations. While the very small Tesla pixel structures meet the BTeV demands for high resolutions, the RD50 investigate the quasi-3D structure's potential of sustaining high efficiencies despite radiation damages (Moll et. al, 2005). I will in the following sub-sections introduce silicon properties that are relevant to my characterizations.

2.a.i SEMICONDUCTORS

Semiconductors are four valence electron elements with conductive properties that differ from conductors and insulators (Woan, 2000). The semiconductors' conductive properties are altered when diffusing so-called impurity atoms into the semiconductor that introduce new charge carriers, called minority charge carriers (Leo, 1994). In p-doped crystals, minority charge carriers, holes, are formed in the vacancies when three valence impurity atoms settle in the silicon crystal (Leo, 1994). By diffusing five valence impurity atoms into the crystal, there will be an excess of electrons that that do not form covalent bonds. These electrons make the minority charge carriers in the n-doped crystals.

2.a.ii REVERSE BIAS JUNCTION

Most silicon detectors are based on the physics of pn-junction. Adjacent n-doped and p-doped regions form a concentration gradient that causes the electrons to diffuse from the n-region to the p-region, but the holes in the opposite direction. This process creates a built-in space charge region, producing a potential barrier that prevents further current flow (Leo, 1994).

An external voltage applied to the pn-junction, changes the net electric field that will alter the volume of the depleted region. If the applied voltage is reversed biased, a positive voltage applied to the n-side, and a negative voltage to the p-side will increase both the volume of the depleted region, and the electric field strength in the silicon (Leo, 1994). These circumstances are exploited in silicon particle detectors. The larger the depletion region, the more space is offered for electron-hole pairs to be produced when charged particles deposit energy along their trajectory (Lutz, 1999). Also, since the intrinsic electric field is larger, the minority charge carriers will be guided more efficiently to the terminals and produce a current signal. A grid consisting of isolated pn-junctions then becomes useful for position measurements of charged particles if each pn-junction has its terminals wire connected to read-out electronics (BTeV).

2.a.iii LEAKAGE CURRENT

Charge carriers find it hard to move around in a reversed biased pn-junction due to the retarding intrinsic electric field. Despite this potential barrier, a small current is detectable (Lutz, 1999). This leakage current creates

a background noise for particle detectors and limits how small of a particle induced signal pulse height the detectors can distinguish. The most significant sources of leakage currents include thermally generated electron hole pairs from the depletion region, and surface effects caused by the surrounding atmosphere (Coluccia, 2002). I kept, for these reasons, track of the temperatures and the relative humidity in order to be assured of a proper laboratory environment when making the current-voltage and capacitance-voltage characterizations.

2.a.iv AVALANCHE BREAKDOWN

The silicon's intrinsic electric field will accelerate the electrons to higher momentum, in between each collision with the lattice atoms, at higher reverse bias voltages. When the reverse bias reaches far beyond the depletion voltage, when the detector area is entirely charge depleted, the momentum transfer in each collision becomes large enough to produce new electron hole pairs (Lutz, 1999). Subsequent collisions cause chain reactions of electron hole pairs, at the onset of this phenomenon called the avalanche breakdown. Very large leakage currents are then produced that may saturate, and permanently damage electronic devices.

2.a.v PUNCH-THROUGH

The doping concentrations become important in the detector structures that I have studied. In order to avoid unwanted effects when the charge depleted region reach the electrodes, a higher doping concentration is

implanted near the electrodes (Lutz, 1999). As the reverse bias increases and the depletion region reaches the p+ region (the plus stands for high doping concentration) that is the side of the source for the detectors that I tested, and before the bias voltage has reached the voltage requirement for avalanche breakdown, a soft breakdown is observed where a current path is open between the source and the drain (Lutz). This procedure, called punch-through, is typical for short channel lengths and occurs when a depletion region connects two p+ implants. The punch-through region behaves as a resistor, hence a linear current to voltage relationship that could be observed in many of my current-voltage measurements.

2.a.vi RADIATION DAMAGE AND SENSOR LIFETIME

Particle irradiation causes damage on the silicon detectors that degrades their performance. Several factors are responsible for this lowering in efficiency, such as:

- Change in the effective ion concentration in the substrate that changes the depletion voltage. Severe radiation damage produces a phenomenon called type inversion, where the effective doping of the substrate changes its sign.
- Increased noise level and temperature due to an increase in the leakage current.
- Signal losses, which charge trappings in the depletion region are responsible for (Garcia).

To satisfy the requirements for detector longevity in the expected radiation dose, the Tesla detectors utilize a process to separate the different n-implants that define individual pixels, called p-spray isolation technique, where a geometrically graded p-dose is diffused between each pixel. A low p-doping dose on the edges to medium dose half-way in between the pixels, minimizes the E-field strength near the edges and results in increased radiation hardness and avalanche breakdown voltage for the detectors (Coluccia, 2002). Contrary to the Tesla detectors, on the other hand, the quasi-3D detectors utilize a certain doping geometry in order to withstand harsh radiation environments.

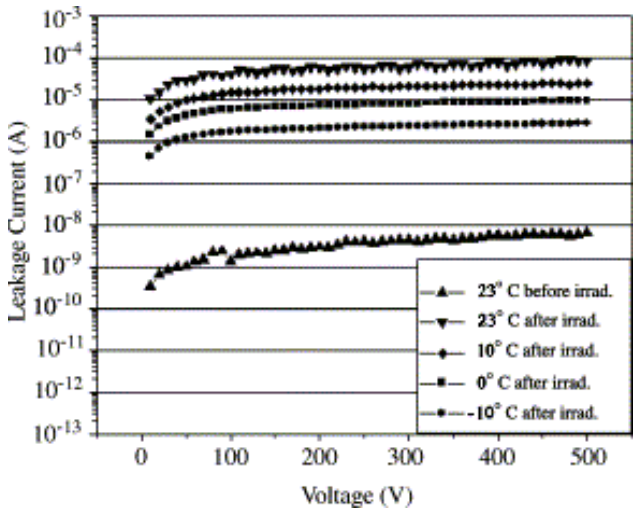

Figure 2: This plot shows how the leakage current is dependent on radiation damage and temperature. The leakage current was increased by several orders of magnitude after irradiation, but was reduced by one order of magnitude when the temperature was lowered by 33°C. These tests were made on prototype sensors on a different wafer than Tesla, utilized a different type of inter-pixel isolation, called p-stop (Artuso, 2002).

2.b BTeV SILICON DETECTORS

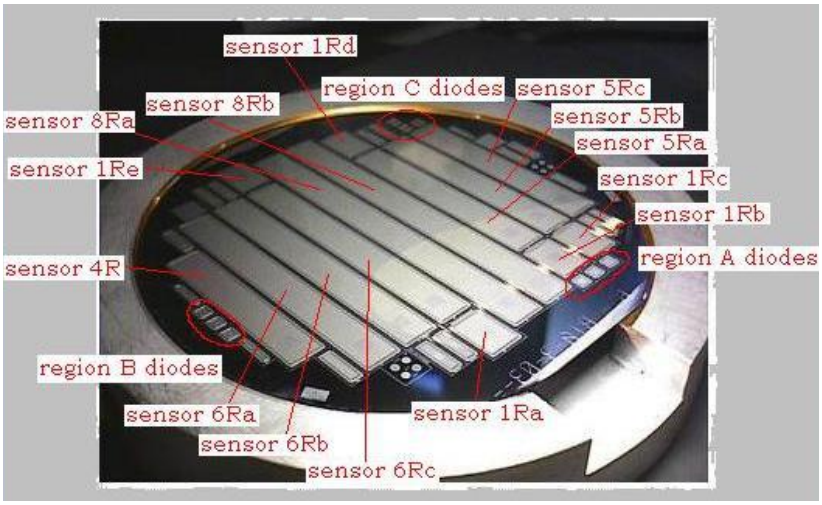

Figure 3: This is the Tesla wafer that I tested in the SU HEP group's clean room facility. I labeled the figure that I copied from (BTeV).

I characterized the Tesla structures labeled in the wafer depicted in Figure 3. The pixel detectors manage a small resolution thanks to the 50x400µm pixel sizes, sufficient to distinguish the closely spaced charged particle tracks right after a p-p collision (BTeV). For the Tesla pixel detectors, the depleted region will grow from the grounded n+ implants such that the electric field reaches the pixels that are connected to electrodes.

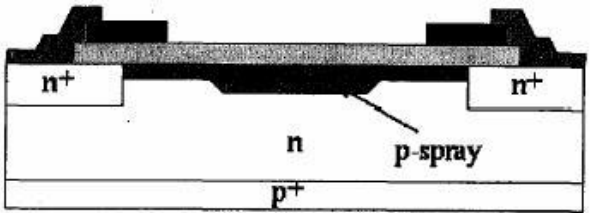

Figure 4: Schematic view of p-spray inter pixel isolation. Depending on the desired geometric extension of the depleted region, silicon doping densities can be altered to suit the requirements. In the Tesla design, the n-bulk had low density while the terminals had higher densities. This prevented the depletion region to reach the electrodes connected to the terminals and cause unwanted effects (Coluccia, 2002). Figure copied from (Coluccia, 2002).

2.c RD50 SILICON DETECTORS

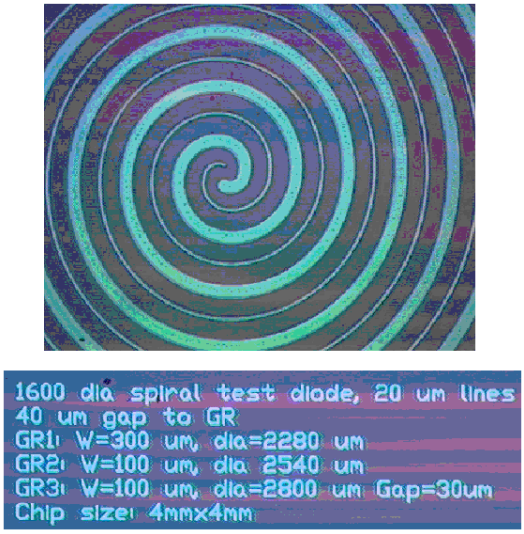

Figure 5: The quasi-3D device is 260µm thick, and the spiral diameter 1600µm. The width of the p+ spiral is 20µm and there is a 30 µm separation between each n+ spiral. Extrapolating from the picture, the width of the n+ spiral should be around 5µm (Bunda, 2004).

The SU HEP is a part of the RD50 collaboration, and made simulations for the quasi-3D structure in order to find its static properties. The development of this new generation of silicon detectors is at an early stage and my measurements contributed to the early nominal bias verifications for these devices. The quasi-3D doping geometry is different from traditional silicon detector structures and has, contrary to pixel detectors, a non-uniform cross section. A p+ spiral closely spaced with an n+ spiral, makes this asymmetric cross section that prevents us from ignoring horizontal components.

2.d ABOUT THE SILICON DETECTOR MEASUREMENT SETUPS

The current-voltage and capacitance-voltage measurements that characterized the silicon micropattern detectors demanded a sophisticated laboratory setup in order to produce valuable data. The measurements took place in a clean room with controlled relative humidity and sensed temperature. Due to the light sensitivity of silicon the silicon structures were placed in a light sealed box that ensured no incoming light. Appropriate

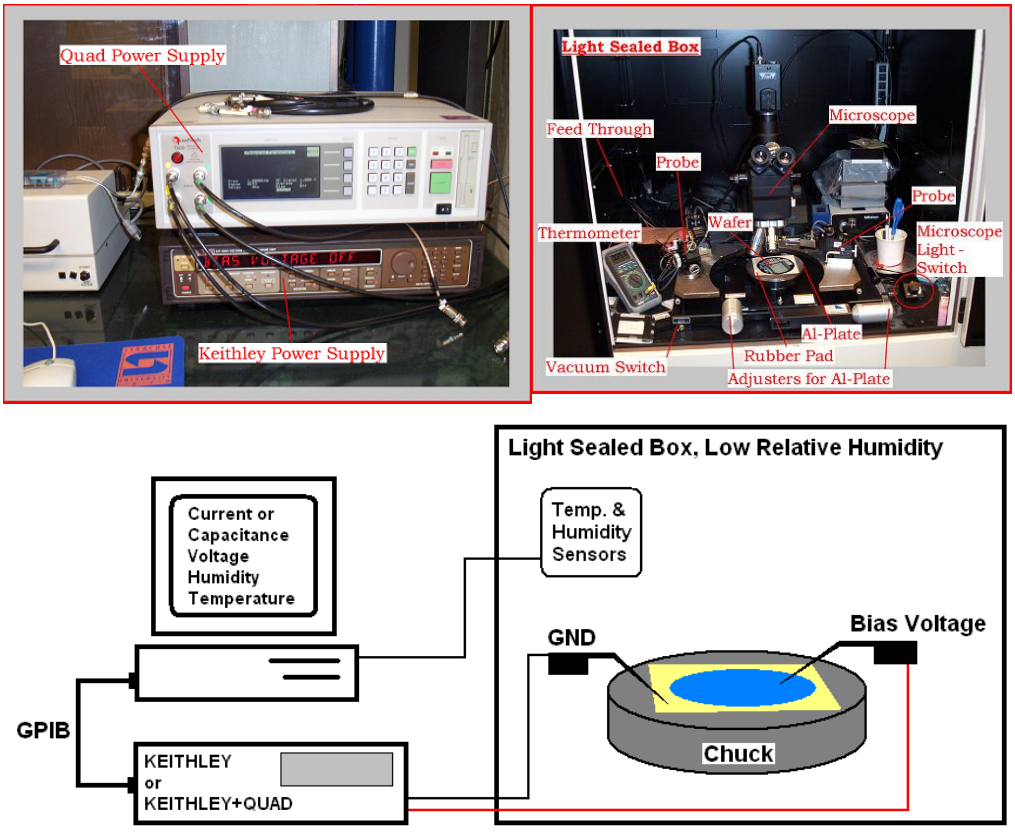

Figure 6: The Keithly Model 237 Source Measure Unit is a power supply (top left) that managed to read currents while sweeping at high voltages. The Quad Tech 7600 Precision LCR Meter Model B (top right) was used to measure the capacitance under different bias voltages and was properly interfaced with the Keithley since it did not manage to sweep at high enough voltages by itself. The small-dimensioned silicon structures demanded microscope assistance (see top right picture) when attaching the biasing pseudo-Kelvin probes. While looking at the microscope, the adjusters moved the aluminum wafer chuck around for proper adjustments to avoid scratching the detectors.

laboratory conditions, created by the SU HEP group, were necessary to produce consistent and reliable test results, as were the detailed procedures on how to go about and take these measurements.

The measurement setup consisted of three main stages: a biasing/sensing stage, a probe station, and the data acquisition (DAQ) stage. The biasing/sensing devices, shown in upper left picture in figure 6, sensed the current response while sweeping the silicon detectors towards greater reverse bias. These devices were connected via tri-axial cables to the pseudo-Kelvin probes in the probe station, that were further attached to the silicon structures on the wafer chuck as seen in the drawing, figure 6. The DAQ stage included Labview software and a PCI that performed DAQ with the information sent to the PC through the GPIB interface. An important feature of these software programs for the current-voltage and capacitance-voltage measurements was a current compliance that shut down the ongoing measurement if the leakage current exceeded a set current limit. Without this feature, I would risk allowing for uncontrolled amounts of leakage currents, caused by avalanche breakdown that could permanently damage the silicon devices.

The pseudo-Kelvin probes were attached to the Tesla structures such that the n+ pixel plane was closed to ground while the p+ back plane was biased with negative voltages. In order to prevent from scratches on the pixel plane, the Tesla wafer was placed on a conductive rubber pad.

For the quasi-3D devices, the grounding probe was connected to the n+ back plane while the p+ spiral was negatively biased. The graphs show positive voltages since I was interested in a log scaled y-axis.

2.d.i ABOUT THE CURRENT-VOLTAGE CHARACTERIZATIONS

The current-voltage measurements consisted of voltage sweeps from zero to avalanche breakdown and served the purposes cataloguing the leakage current response. In order to gain a better understanding of the optimal bias configurations, it was important to retrieve the leakage currents for the different devices, as well as knowing the onset of avalanche breakdown.

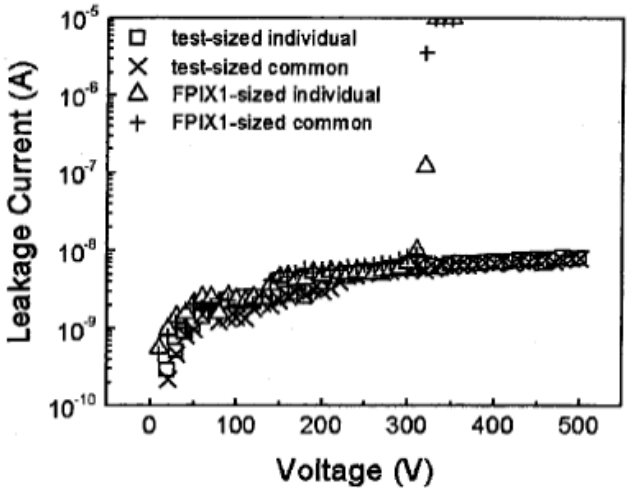

Figure 7: This is a Current-Voltage characteristic for un-irradiated p-stop pixel detectors. The graphs show silicon devices that sustain high reverse bias before avalanche breakdown occurs, seen by the steep increase in leakage current. Figure copied from (Coluccia, 2002).

2.d.ii ABOUT THE CAPACITANCE-VOLTAGE CHARACTERIZATIONS

Capacitance-voltage measurements were important in order to retrieve the onset of the depletion voltage. The applied voltage was swept towards larger reverse bias beyond the depletion voltage. Figure eight, next page, shows how the depletion voltage is retrieved for the Tesla structures.

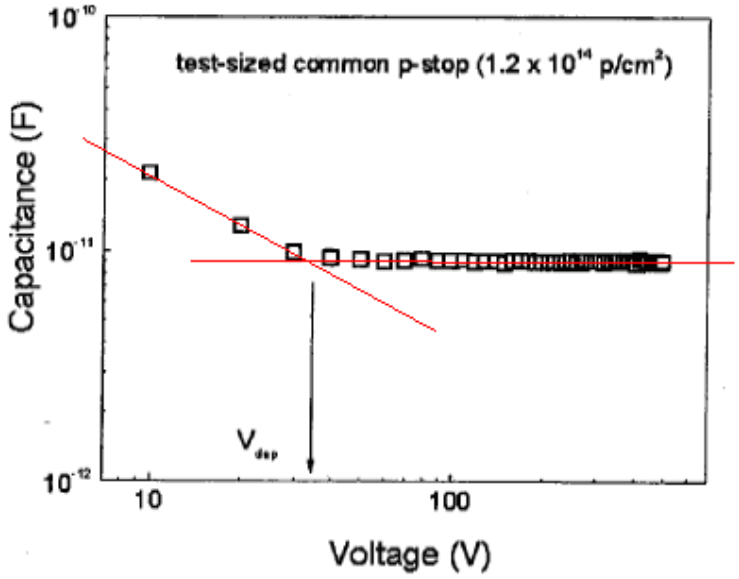

Figure 8: The depletion voltage can be retrieved from the capacitance-voltage characterizations at the point where the capacitance stops decreasing. Figure copied from (Coluccia, 2002).

As the bias voltage increases, the space charge region increases and the distance between the edges of the depletion layer will increase. Since the capacitance is proportional to the area/distance (Woan, 2000), and the area is kept constant, the capacitance will decrease. Eventually the n-bulk becomes fully depleted and the distance will increase (into n+ implant) at such a small rate that we can think of the capacitance as becoming constant. The depletion voltage has been reached and is extracted from the CV characteristics by

finding the intersection of the fitted straight lines in the plot with logarithmic values.

2.e Tesla MEASUREMENT RESULTS

The different the different breakdown voltages for the Tesla structures are summarized in Table 2 in the appendix. The current-voltage graphs (also in the appendix), on the other hand serve as a catalogue of the different leakage currents under different bias voltages. It is important to note that the repeatability in my measurements was confirmed by abundant tests that I took under different occasions spanning up to one year.

I determined that my measurements verified an expected independency on the relative humidity (%RH) for the Tesla pixel detector structures. Measurements made at Fermilab showed similar properties for values between 0 and 40%RH (Coluccia, 2002). Two current-voltage (I-V) graphs for the Tesla 8Ra structure is one part of my verification that shows how the breakdown voltages and leakage currents are the same despite the large %RH difference.

The Labview software allowed me to vary the step sizes for the voltage sweeps, and I noticed that an increased step size caused pronounced punch-through effects. The Tesla 5Rb and 6Rb I-V graphs demonstrate this effect for different step sizes that can be explained by the larger shortening effects that are caused by the more sudden changes in bias voltages. The same graphs are two examples that show that the onset voltage for avalanche breakdown is not affected by the step size. This allows us to rely on the

breakdown voltages presented in Table 2, despite the different step sizes that were used.

The punch-through is easier to observe on some graphs more than others but should match the depletion voltages from the capacitance-voltage measurements. This was the case for 5Rb, 6Rb, and 8Rb.

The way the Tesla pixel detectors were developed allowed for smoother current-voltage progressions than for the diode structures. I also observed from my measurements that the relative humidity had a large impact on the leakage current and the breakdown voltage. This behavior was different from the pixels' and shows the importance of appropriate lab conditions. Chart 20 for the Region C diodes, shows the avalanche breakdown independency of the step size.

The high breakdown voltages confirm that the structures are suitable for high energy particle detectors. Exceptions are detectors 1Rb, 6Rc, and 8Ra that have different onsets of breakdown due to lateral current effects between the pixels. The same type of breakdown onset was observed in the quasi-3D I-V characterizations.

The capacitance-voltage measurements point, for the Tesla pixel detectors, out the depletion voltages, the onset of the punch-through effect.

2.f Quasi-3D MEASUREMENT RESULTS

The I-V characterizations showed a smoother onset of avalanche breakdown due to lateral current effects between the p+ spiral and the n+ spiral. The same type of breakdown onset was observed in the I-V characterizations for the Tesla 1Rb, 6Rc, and 8Ra structures. What I also noticed was that the same Tesla structures had very similar C-V characteristics as the quasi-3D structures, probably also due to the lateral current effects.

The I-V characterizations on the quasi-3D "Bottom" structure, indicate strong step dependency, which was not a surprise due to their strong lateral current effects.

The Quasi-3d "Right" indicated strong humidity dependence. This was not a surprise considering their small sizes.

Best results were given when back plane was closed to ground. The current-voltage and capacitance-voltage measurements were consistent with previous measurements at Purdue (Roy, 2004).

3. BTeV RICH INSTRUMENTED MaPMT CHARACTERIZATION

A crucial step in detector construction is the bench test of detectors connected with their dedicated front-end electronics. I had the opportunity of performing this study with the Multi Anode Photomultiplier Tubes (MaPMT), chosen as the single photon detectors in the BTeV gas radiator Ring Imaging Cherenkov (RICH) detector, attached to their own custom made electronics. Both the MaPMTs and the front-end electronics are unique and novel devices, developed specifically for our application.

Figure 9: The MaPMTs for the BTeV RICH detector were developed by Hamamatsu. (Blusk)

3.a INTRODUCTION TO READOUT RESPONSE MEASUREMENTS

In the electronics calibration, signals of comparable amplitudes to the ones coming from the MaPMT were injected to the ASIC input channels in order to mimic the signals from the BTeV RICH during the real experiment. The readout of the electronics is binary; however, our version of the ASIC features a test channel with analog output that is useful for diagnostic purposes. I used this analog output to establish the MaPMT signal range under nominal operating conditions. The goal was to verify the extent to which the dynamic range of the preamplifier, and that the shaper were matched to the MaPMT gain. In particular, a concern was the fraction of events that registered saturated outputs, caused by input signals that exceeded the linear dynamic range of the analog portion of the ASIC, as they were the source of considerable cross talk. Thus, I measured the fraction of saturated analog ASIC outputs under bench test conditions similar to the ones in the beam test of this apparatus that took place in January 2005. Both pulse generated signals and MaPMT signals were passed to the ASIC to make these quality measurements calibrated.

3.b DEVICES UNDER TEST

The key devices in my analog characterizations were the MaPMT, the MaPMT baseboard, and the Front End Hybrid. Followed is a brief introduction to their properties before I move on explaining how they are interfaced for the readout response measurements.

3.b.i MULTI ANODE PHOTO MULTIPLIER TUBE

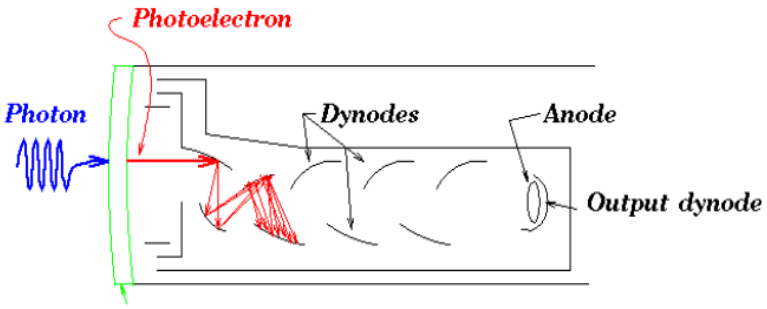

Figure 10: This drawing, copied from (Blusk), shows the schematic of one channel in the MaPMT.

Each MaPMT consists of three major components: the photocathode, the dynode string, and the output dynode (anode). The MaPMT has its window coated with a photocathode that is sensitive to blue light (Cherenkov radiation is in the blue region) (Leo, 1994). When an incident photon strikes the photocathode, an electron is ~25% likely to be emitted by the photoelectric effect (Blusk). Since a high voltage is applied to the MaPMT, the photoelectron is further accelerated through a strong electric field towards the output dynode (see figure 10). On its way through the dynode string, the photoelectron will strike the 12 dynode-stages and each time knock off additional electrons. A gain of ~10^6 electrons eventually reach the output

dynode that creates a semi-Gaussian shaped MaPMT pulse as seen in figure 11 (Blusk). The pulse height is in the order of 10-30 mV and has a pulse width of ~10 ns.

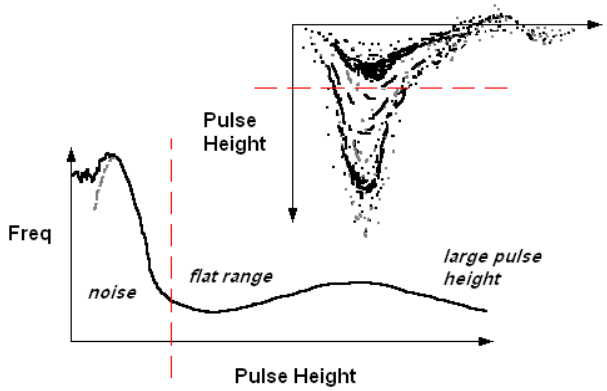

Figure 11: The semi-Gaussian shaped MaPMT pulse is represented on the upper right corner of the figure, and the lower left part of the figure shows its pulse height distribution. It is important that the frequent thermally emitted noise signals have lower pulse heights than that of the output pulse signals from the detected photons.

The greatest source for the MaPMT background noise, is thermally emitted electrons that become accelerated through the strong electric field. Since these signals have lower pulse heights than that of the output pulse signals from the detected photons (see figure 11), the photon-induced signals are not lost when triggering pulse heights that are greater than the noise levels.

3.b.ii FRONT END HYBRID AND THE ASIC

A total of 16 MaPMTs can be mounted on each MaPMT baseboard that is responsible of proper high voltage distribution across the dynode strings in the MaPMTs. Eight out of these MaPMTs are connected to the same ASIC on the Front End Hybrid (FEH), that contains two ASICs, via two 32-parallel wire cable with Samtec connectors. Each cable line is routed to one

input channel in the front-end ASIC. The final input connections are made through wire bonds.

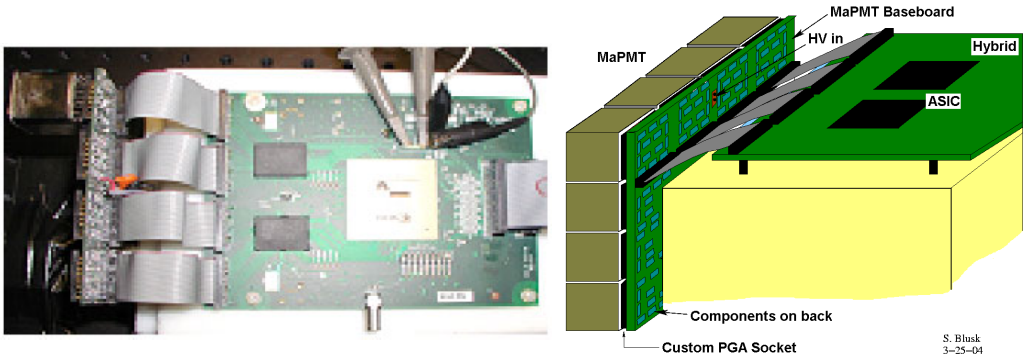

Figure 12: The drawing, a modified copy from (Blusk), maps out what is seen is seen in the photograph to the left. Each MaPMT will have its signals routed to one of the two ASIC (two black rectangles on the photograph to the left) depending on where on the baseboard it has been mounted.

Data Acquisition (DAQ) is not possible without the ASIC since it is capable of processing the MaPMT current signals into digital outputs. Each ASIC has 64 channels that can process a current signals through three stages. First, the injected current signal encounters a semi-Gaussian charge sensitive preamplifier that essentially pronounces the pulse height. A shaper that eases further signal manipulation by refining the pulse shape then further processes the signal. If this signal exceeds an externally programmable threshold, a binary signal, digital output, is produced in the corresponding channel. An important feature is the analog test channel that allows observations of the semi-Gaussian response to an input signal, whose size is dependent on the time-over-threshold (Blusk). In my measurements, I studied this response by injecting both pulse generated and MaPMT passed signals into the ASIC. The MaPMT current signal was injected directly into “MAPMT INPUT” and was

further processed by the charge sensitive preamplifier. Since the signal generated by the pulse generator is a voltage signal, it had to be transformed

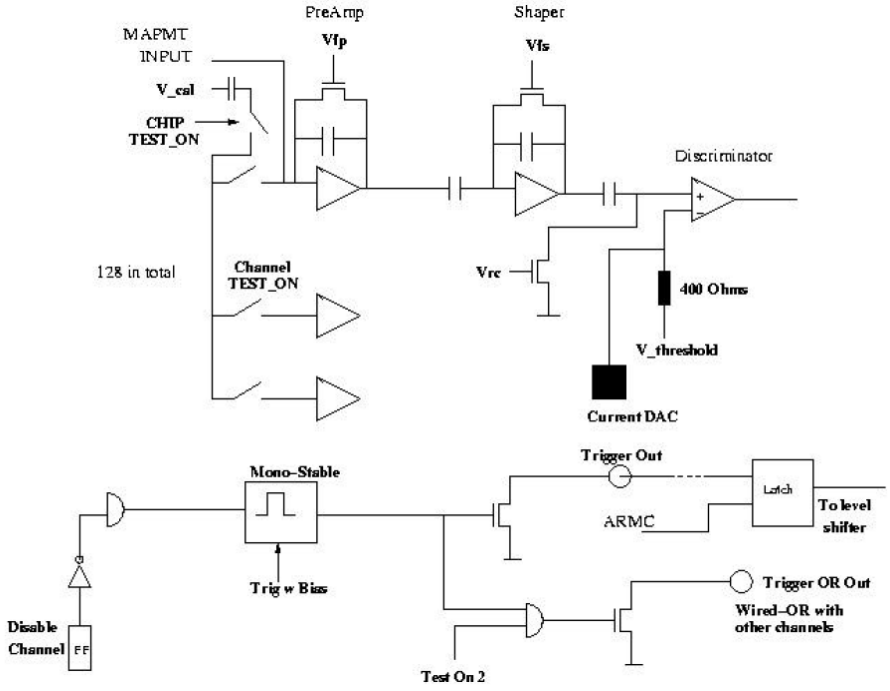

Figure 13: The schematics represent the ASIC that consists of 64 identical amplifier-shaper-discriminator circuits according to the circuitry above. Optimal, software controlled, preamplifier and shaper voltages, V_{fp} and V_{fs}, helps the discriminator to output a narrow digital square pulse. (Blusk)

into a charge pulse, or current signal. By enabling "V_cal" in the ASIC with the software, the voltage signal was processed into a current signal by a voltage divider and a capacitor before reaching the preamplifier (Blusk).

3.c DEVICES UNDER TEST INTERFACED

The pulse generator output two synchronized signals. The 25μs TTL signal triggered the PTA for DAQ from the Hybrid, while the synchronized pulse was sent either directly to the Calibration Input or to the LED. The analog ASIC response was measured with both setups by enabling Analog Output in the software that allowed PTA/MEZZANINE to talk to the Hybrid

and make other configurations software controllable, such as thresholds, V_{fp} and V_{fs} besides from enabling analog out. The PC communicated with the PTA/Mezzanine card via the PCI (Blusk).

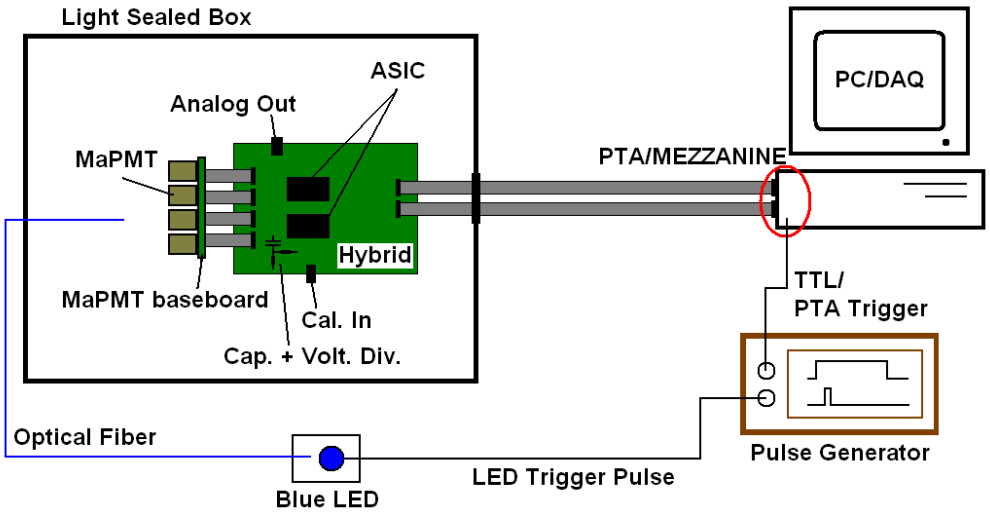

Figure 14: A block diagram that maps out the different components of the measurements. The Pulse Generator outputs 4kHz pulses for our measurements.

3.d PULSE GENERATED ANALOG OUT

The pulse generator generated pulses with consistent pulse widths and pulse heights. If the signal has the right bias configuration, it would mimic the MaPMT output but with a consistent shape and this was utilized in order to make calibrating tests by observing what injected signal shapes caused saturated ASIC outputs. The analog ASIC output was a good indication of saturated signals. The pulse generator output was connected directly to the Calibration Input, and further through the 1/10 voltage divider and a 1pF capacitor. By the Q=CV relation, the amount of injected charge to the preamplifier was controlled by varying the pulse height and pulse width of the pulse generator output (Blusk).

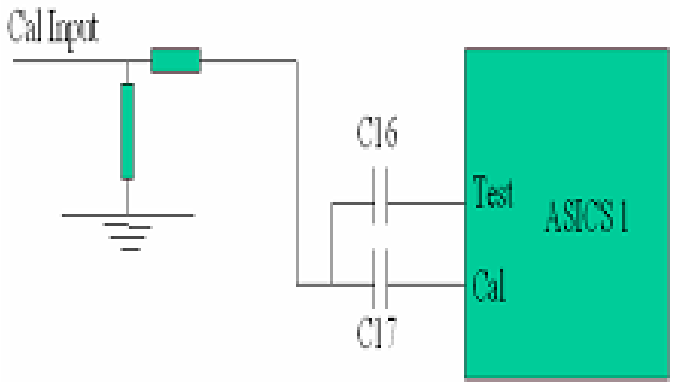

Figure 15: The ASIC setup for pulse generated analog out calibration.

3.e MaPMT GENERATED ANALOG OUT

After calibration, the readout response measurements were with single photon generated MaPMT signals passed to the ASIC. This type of measurements provided to the front-end electronics with a signal environment identical to real particle detection as long as single photon LED pulses were obtained. The pulse generator signal triggered the LED that sent subsequent light pulses through an optical fiber. The optical fiber, that was fed through the light sealed box (see figure 14), and was directed and collimated to whatever MaPMT pixel that was connected to the calibrated input. The optimal way to obtain 1 photon on average was not only a collimated fiber but also by, in my case a 20ns wide LED activation pulse. The narrow pulse allowed more realistic triggering configuration, as the arrival time of the photon was well defined, similarly to what happens in the experimental condition when the beam-crossing clock determines the time of the collision.

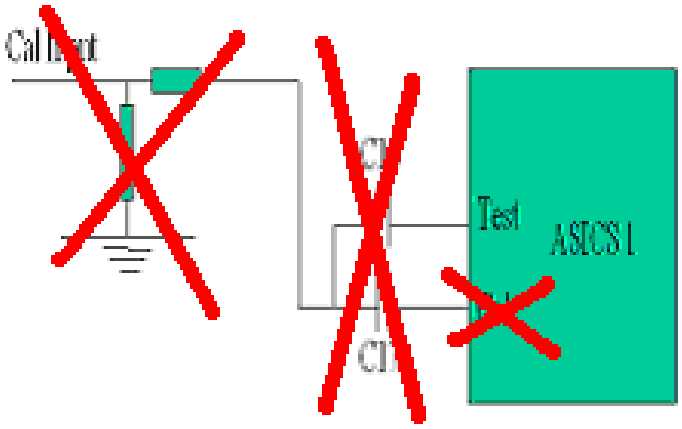

Figure 16: Since the MaPMT is a current signal, it skips the capacitor stage before reaching the ASIC.

3.f READOUT RESPONSE MEASUREMENT AND RESULTS

In the beam test that took place in January 2005, three MaPMT types were used for the BTeV RICH detector. The MaPMTs were identified with the three different gain ranges shown in table 1, and I implemented the single photon source first after calibrating the tubes under the nominal operating voltages also seen in table 1. The calibration made with the pulse generated input setup described in section 3.d, and by taking snapshots of the MaPMT output that revealed whether we saw single photon events (see figure 18) or not (see figure 19).

Device	Gain Range	Nominal Operating Voltage
ZA1923	3-4*10e6	700
NA0068	2-3*10e6	750
NA0048	1-2*10e6	800

Table 1: The three devices that were used in my measurements had three different gain ranges, hence the different nominal operating voltages. The low gain devices, e.g. NA0048, needed higher operating voltages such that they would reach the same gain as the high gain devices, e.g. ZA1923.

By taking snapshots of the analog output response from the semigaussian shaper on the oscilloscope, see figures 20-25, I was able to obtain the fraction of saturated analog ASIC outputs (see figure 22) under similar bench test conditions to the ones in the beam test.

Important to note about my measurements was that the method of using an oscilloscope as the means to observe single-photon induced MaPMT signals (see figure 21), required that the oscilloscope was properly triggered above noise levels. The trigger values in tables 3-5 matched the noise signal

study I made by taking snap shots of the MaPMT noise (see figure 20) and by setting the oscilloscope trigger above these pulse height values.

The pulse height distributions that I retrieved from these measurements revealed small fractions of saturated signals (see chats 40-42), hence I was able to verify that both the dynamic range of the preamplifier, and the shaper-configuration were properly matched to each MaPMT gain.

4. FINAL REMARKS

I had the chance to do research on the two key elements of experimental particle physics: advanced position sensitive detectors, and front-end electronics. In particular, it was exciting to work with novel detectors, which were the first world implementation of this single photon detection technique.

It was gratifying to see single photons in my apparatus and to be able to contribute to the Syracuse University High Energy Physic Group with the pulse generator.

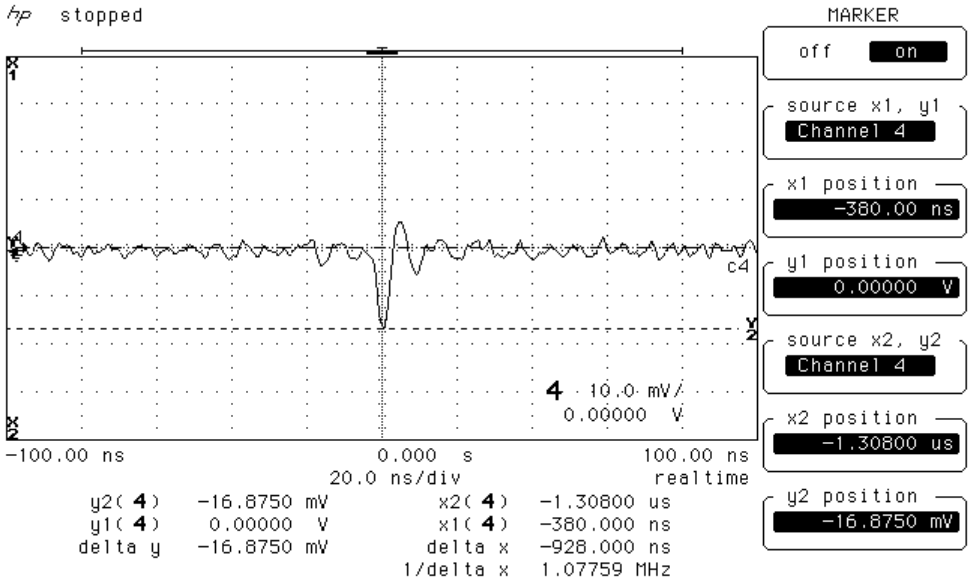

Figure 17: A single photon observation I made using the NA0068 MaPMT and an oscilloscope.

REFERENCES

Books

Lutz, G. (1999). *Semiconductor radiation detectors: device physics (accelerator physics)*. : Springer-Verlag.

Leo, W. (1994). *Techniques for nuclear and particle physics experiments: a how-to approach*. 2nd ed. : Springer-Verlag.

Woan, G. (2000). *The Cambridge handbook of physics formulas*. : Cambridge University Press.

Journals

Cronin, J., Christenson J., Fitch V., and Turlay, R. (1964). *Physics Review Letter*, *13*(138).

Moll, M. (2005). Development of radiation tolerant semiconductor detectors for the SUPER-LHC. *Nuclear Instruments and Methods A*, INN PRESS

Coluccia, M. R., Appel J., Chiodini G., and Kwan, S. (2002). Iv and cv curves for irradiated prototype btev silicon pixel sensors. *Fermilab-Conf*, *02*(148-E), 1-6.

Web-pages

Garcia, S. (n.d.). Charge collection for irradiated p+n si detectors. Retrieved Apr. 27, 2005, from http://www.physics.purdue.edu/vertex/talks/marti.pdf.

Artuso, M. (2002). The btev pixel detector system . Retrieved Apr. 27, 2005, from http://www.sciencedirect.com/science?_ob=ArticleURL&_udi=B6TJM-47GXX13-5&_coverDate=03%2F21%2F2003&_alid=186507782&_rdoc=1&_fmt=&_orig=search&_qd=1&_cdi=5314&_sort=d&view=c&_acct=C000043272&_version=1&_urlVersion=0&_userid=783137&md5=b864ab50026f63a750ab95dfb4d95201.

Blusk, S. (n.d.). Retrieved Apr. 27, 2005, from MAPMT Activities at Syracuse Web site: http://www.physics.syr.edu/~sblusk/mapmt/index.html.

Fermilab, (n.d.). Particle matter - physics at high energy. Retrieved Apr. 27, 2005, from http://www.fnal.gov/pub/inquiring/timeline/index.html.

BTeV, (n.d.). Why BTeV?. Retrieved Apr. 27, 2005, from http://www-btev.fnal.gov/public/gen/index.shtml.

Bunda, N. (2004). BNL semi-3D Test Diode. Retrieved Apr. 27, 2005, from http://www.physics.purdue.edu/usrd50/BNL_semi-3D/test_diode/

Roy, A. (2004). Semi-3D Diode. Retrieved Apr. 27, 2005, from http://www.physics.purdue.edu/usrd50/talks/Semi_3D_Diodes_Initial_IV_measurement.ppt

APPENDIX

A1. Tesla Characterizations

Tesla I-V and C-V Measurements, Reverse Bias				
	Tesla I-V Measurements			Tesla C-V Meas.
	V(break) (V)	I(leak) (nA)	Obs. Punch-Through(V)	V(dep) (V)
1ra	-720	50	N/A	-158
1rb	-90	17	N/A	-100
1rc	-220	10	-110	-142
1rd	-910	50	N/A	-166
1re	-630	50	N/A	-166
4r	-470	50	N/A	-150
5ra	-550	3500	N/A	-160
5rb	-195	22	-95	-102
5rc	-90	90	N/A	-155
6ra	-80	70	N/A	-178
6rb	-150	50	-80	-86
6rc	-500	130	N/A	-148
8ra	-220	75	70	-128
8rb	-460	350	150	-122
Region A Left	-855	11	N/A	N/A
Region A Center	-815	5	N/A	N/A
Region A Right	-815	7	N/A	N/A
Region B Top	-780	10	N/A	N/A
Region B Middle	-720	28	N/A	N/A
Region B Bottom	-510	15	N/A	N/A
Region C West	N/A	N/A	N/A	N/A
Region C Center	-870	20	N/A	N/A
Region C South	-870	26	N/A	N/A

Table 2: This table lists the Tesla measured avalanche breakdown voltages, leakage currents at onset of avalanche breakdown, and the observed depletion voltages wherever applicable, from the I-V characterizations. The depletion voltages, retrieved from the C-V characterizations, are listed for the pixel detectors. C-V measurements on the diode structures were never retrieved.

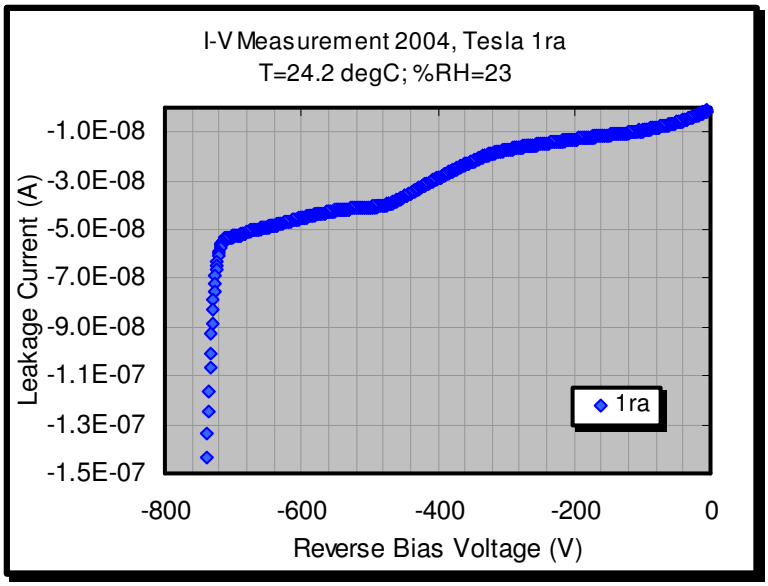

Chart 1: Avalanche breakdown occurred at –720V.

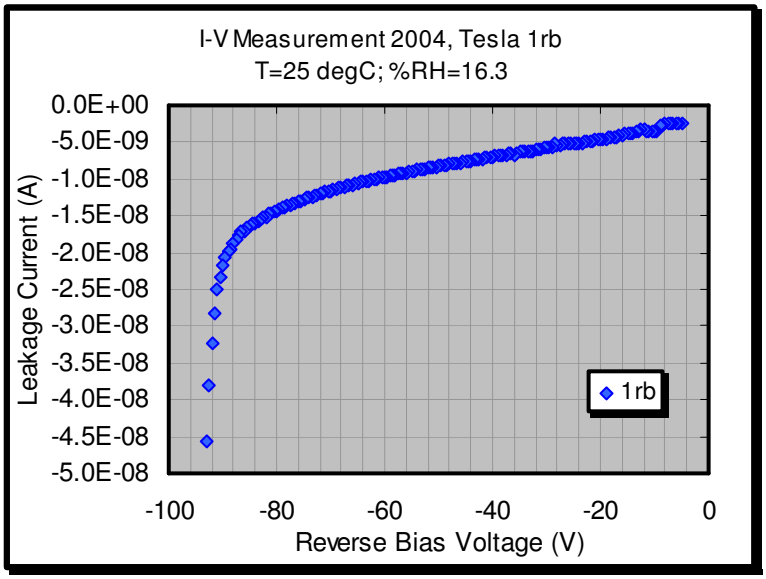

Chart 2: A soft avalanche breakdown was introduced at –90V.

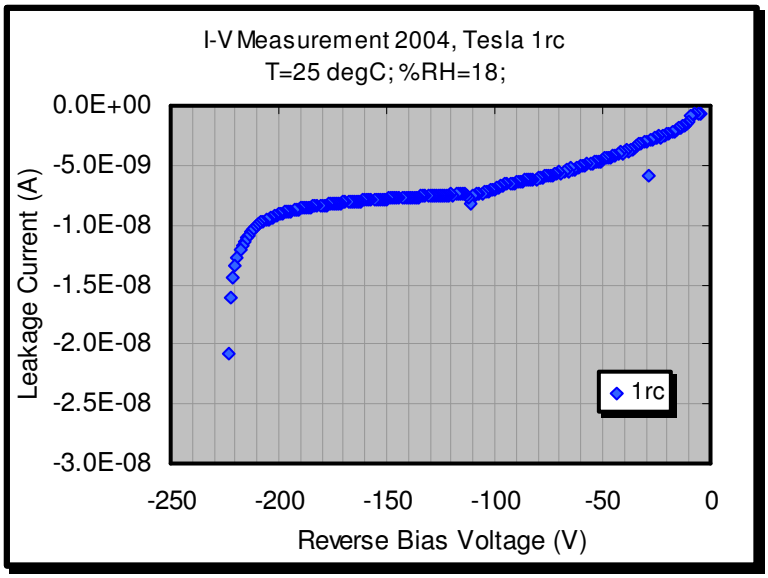

Chart 3: Avalanche breakdown occurred at –220V and a punch-through effect was observed at –110V.

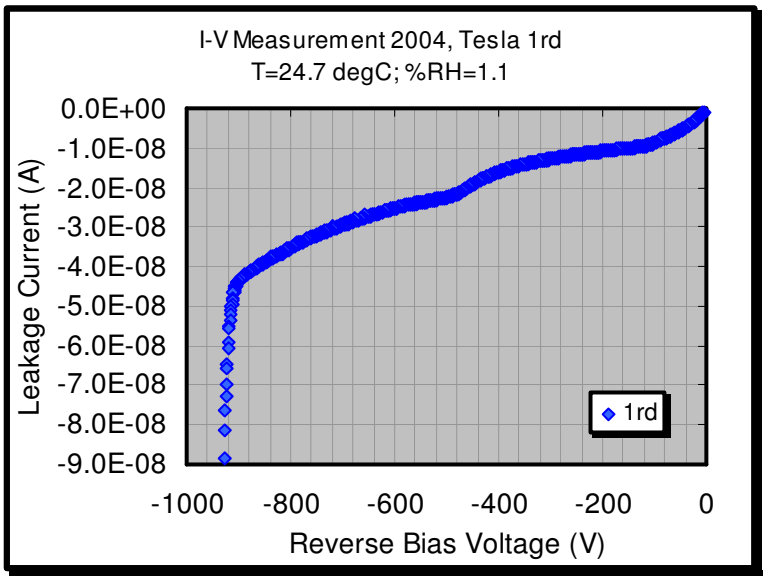

Chart 4: Avalanche breakdown occurred at –910V.

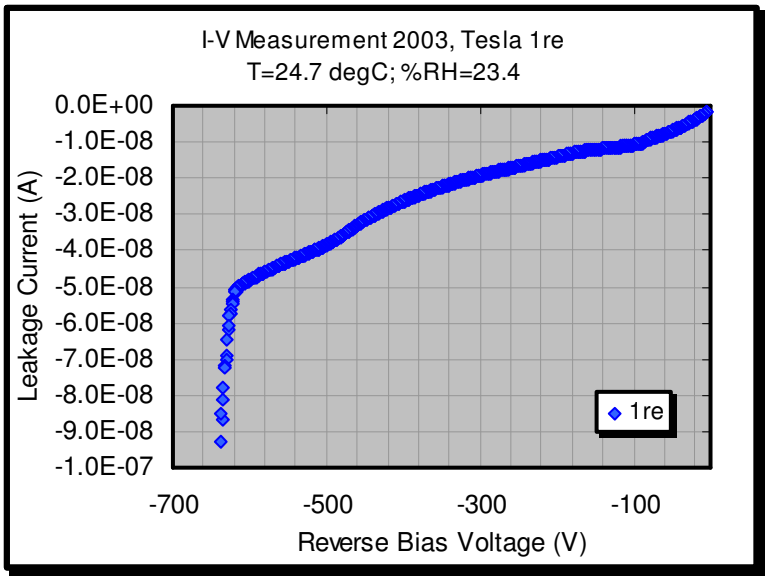

Chart 5: Avalanche breakdown occurred at –630V.

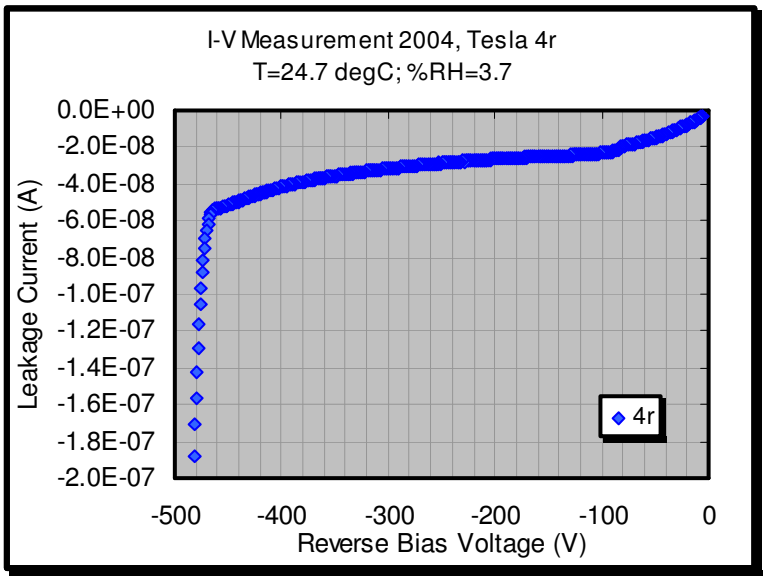

Chart 6: Avalanche breakdown occurred at –470V.

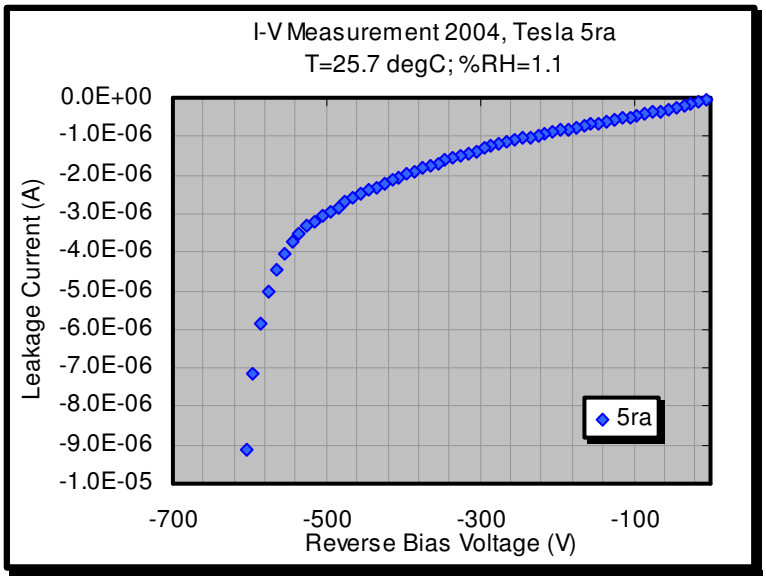

Chart 7: Avalanche breakdown occurred at –550V.

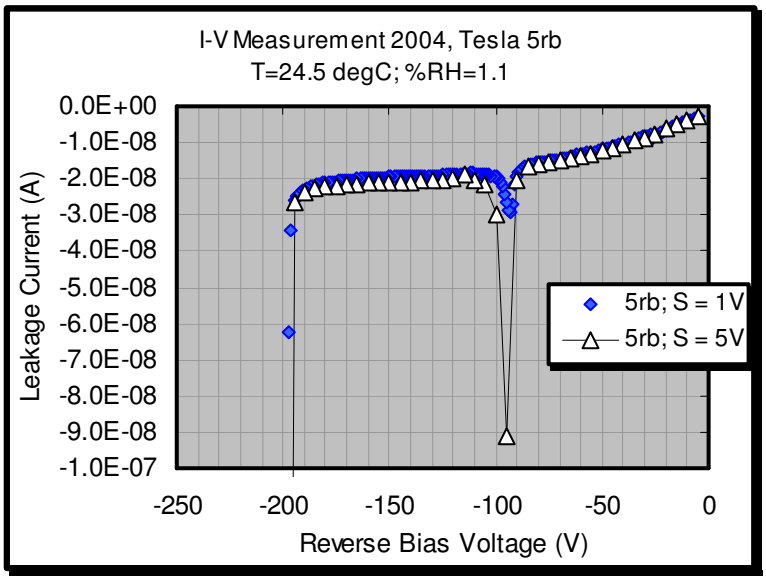

Chart 8: Avalanche breakdown occurred at –195V and a punch-through effect was observed at –90V.

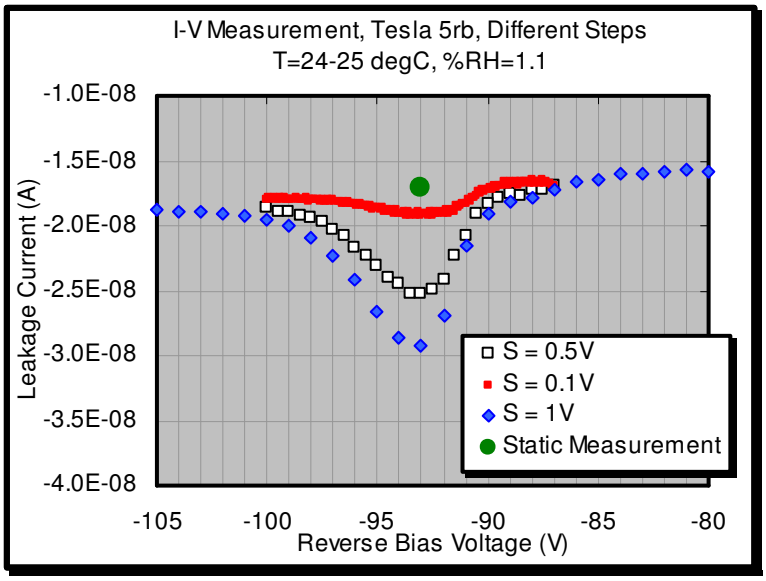

Chart 9: This graph demonstrates more pronounced punch-through effects as the step sizes become larger.

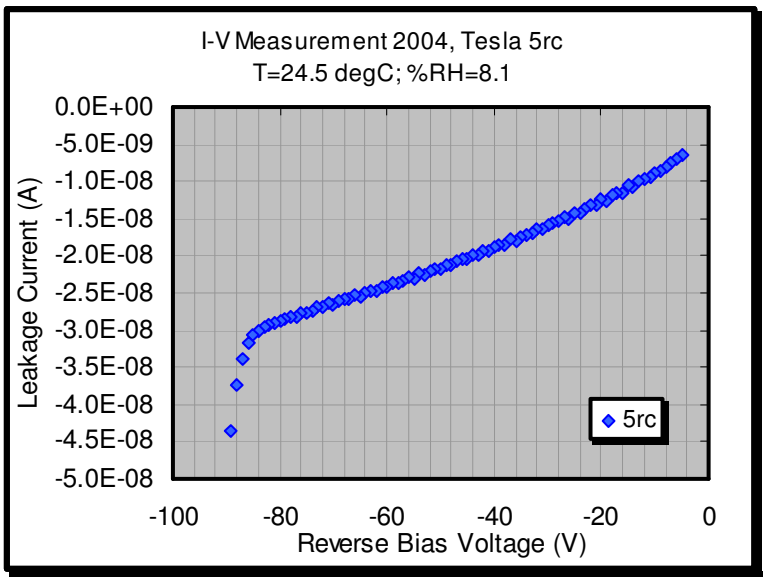

Chart 10: Soft avalanche breakdown effect that occurred at –90V.

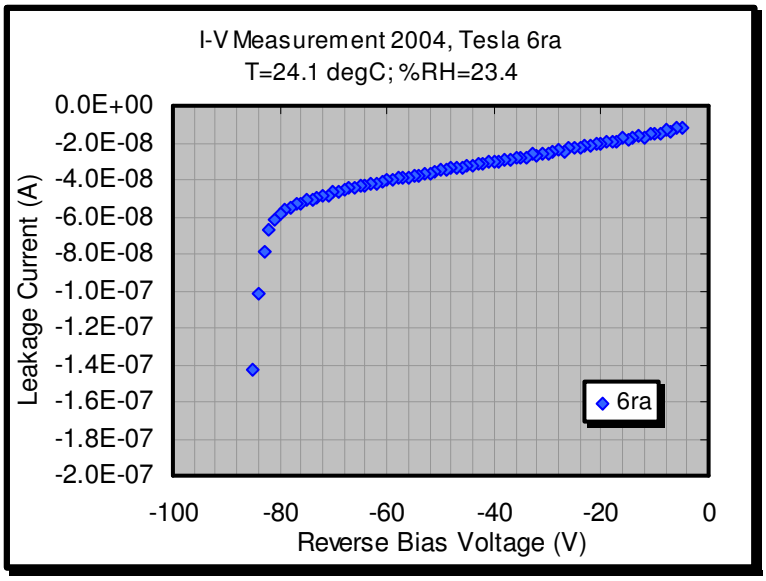

Chart 11: Soft avalanche breakdown effect that occurred at –80V.

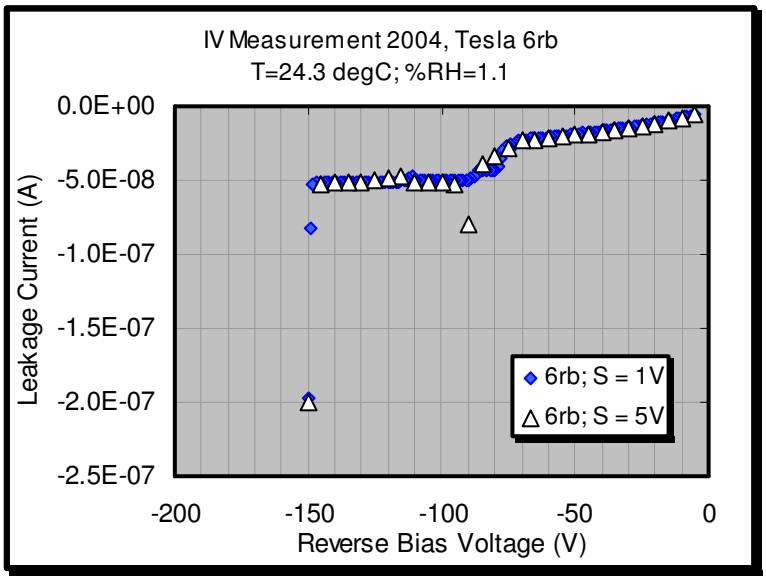

Chart 12: Avalanche breakdown occurred at –150V and a punch-through effect was observed at –80V.

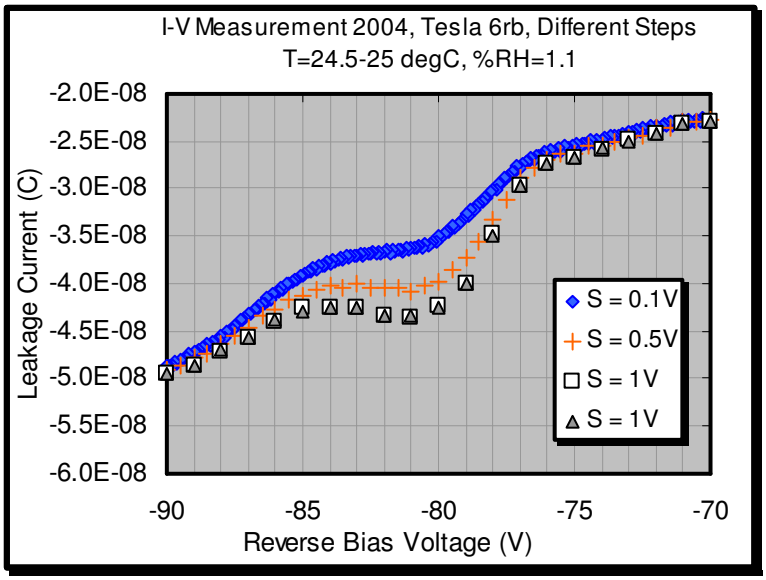

Chart 13: This graph demonstrates more pronounced punch-through effects as the step sizes become larger.

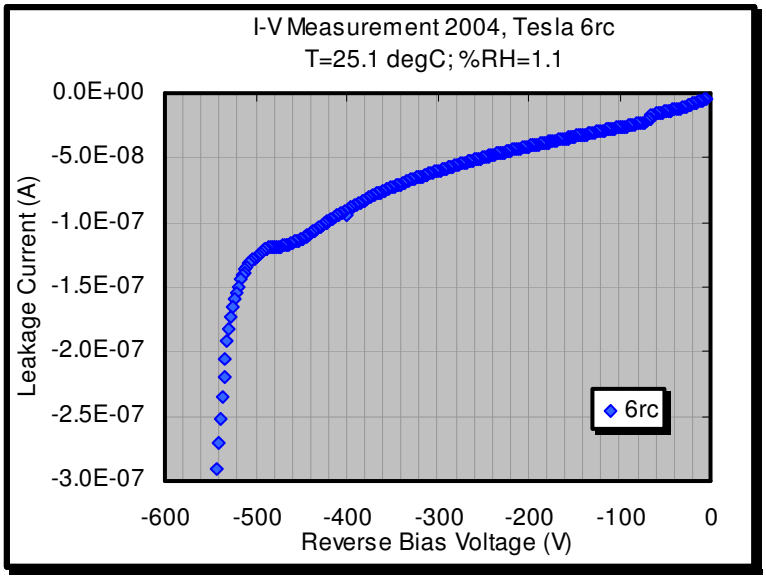

Chart 14: Avalanche breakdown occurred at –500V.

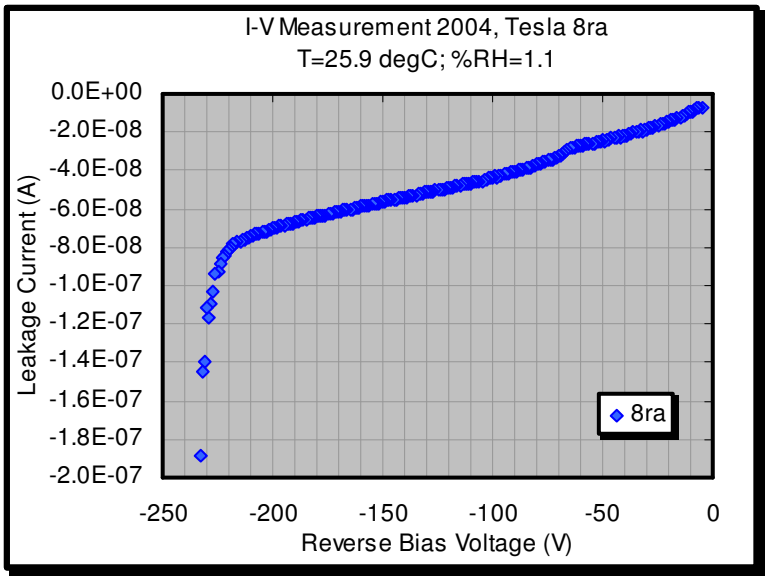

Chart 15: Avalanche breakdown occurred at –220V for low relative humidity.

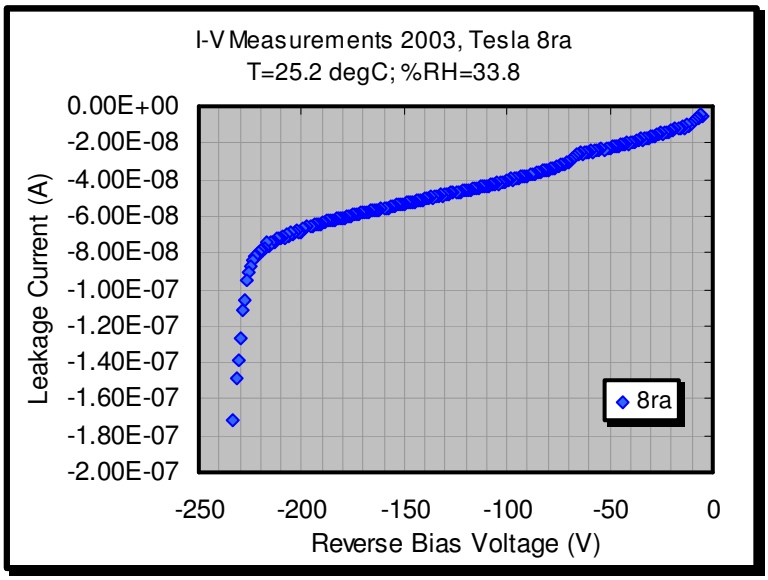

Chart 16: Avalanche breakdown occurred at –220V also for high relative humidity.

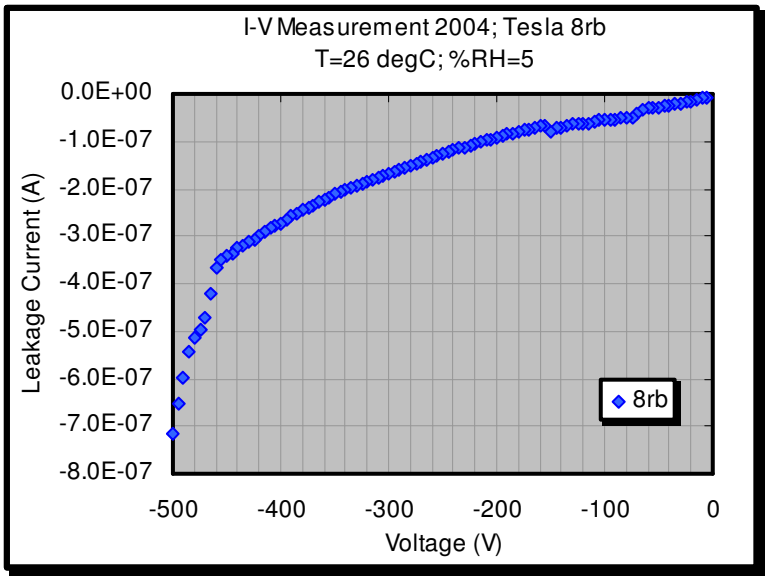

Chart 17: Avalanche breakdown occurred at –460V.

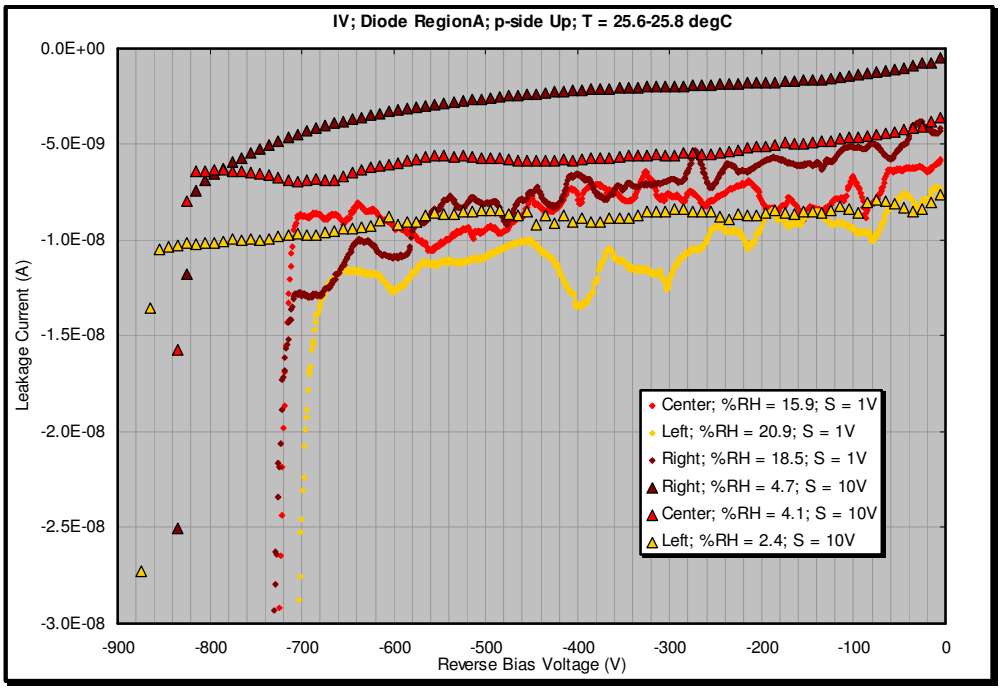

Chart 18: The different breakdown voltages, stated in Table 2, are based on the measurements with low relative humidity (%RH) due to the diode structure's strong humidity dependence.

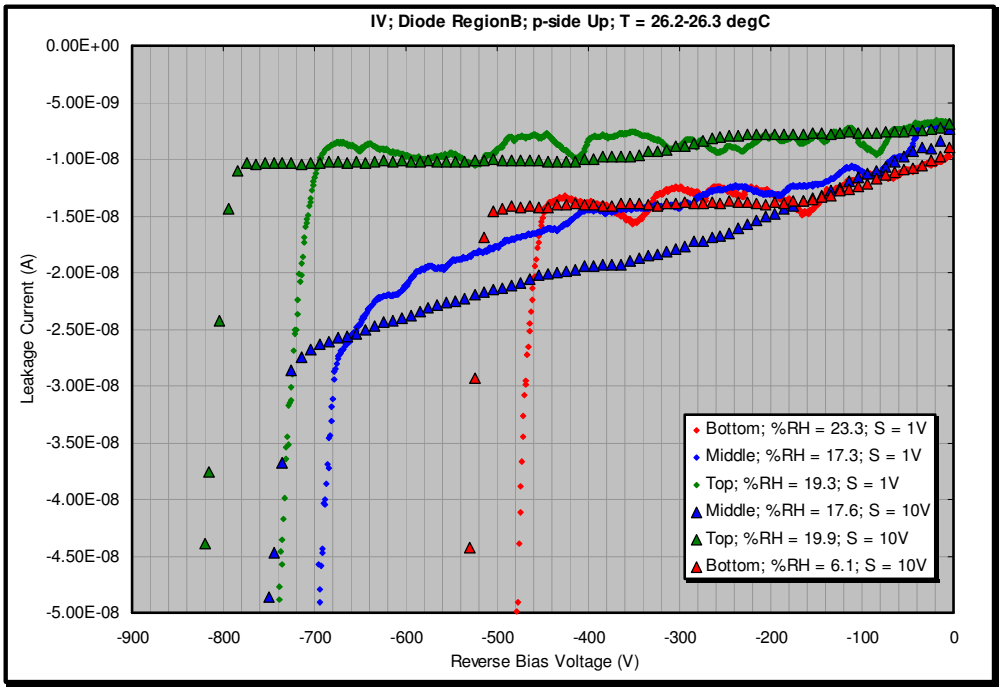

Chart 19: The different breakdown voltages, stated in Table 2, are based on the measurements with low relative humidity (%RH) due to the diode structure's strong humidity dependence.

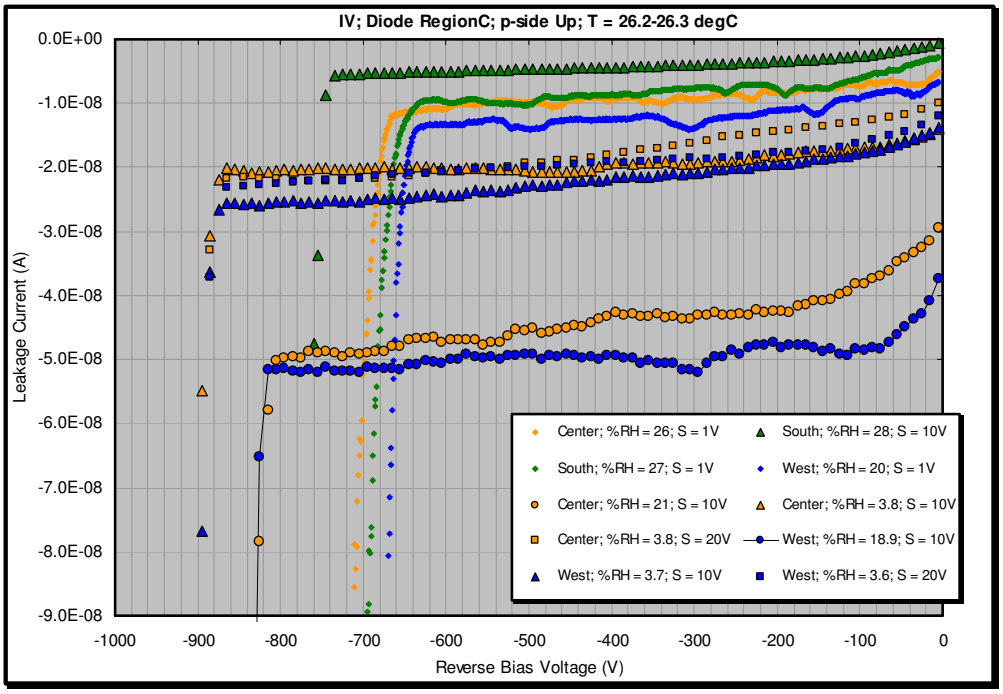

Chart 20: The different breakdown voltages, stated in Table 2, are based on the measurements with low relative humidity (%RH) due to the diode structure's strong humidity dependence.

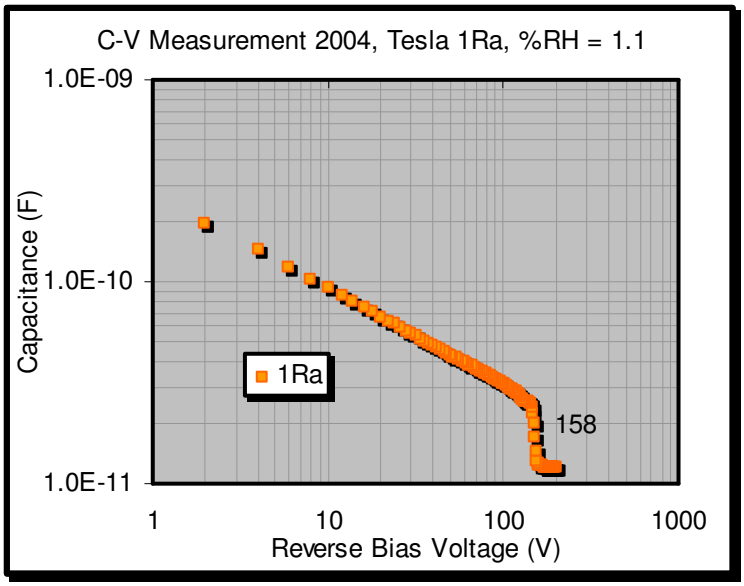

Chart 21: The measured depletion voltage was -158V.

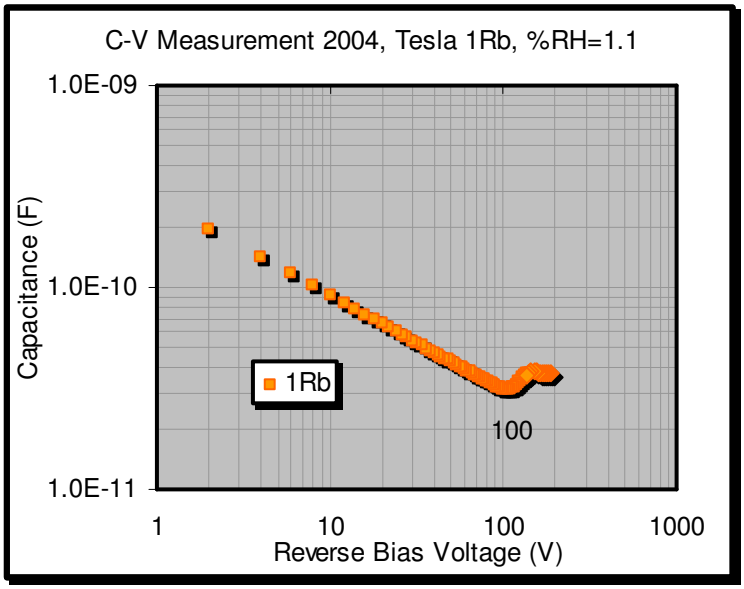

Chart 22: The measured depletion voltage was –100V.

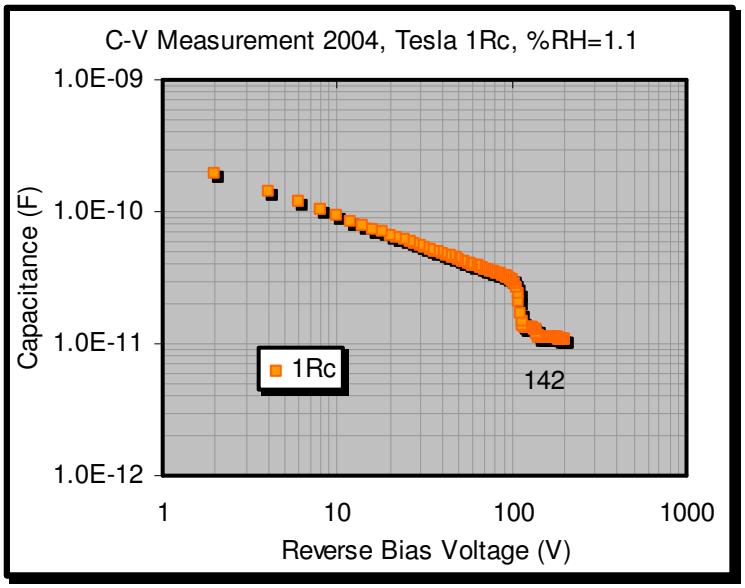

Chart 23: The measured depletion voltage was –V.

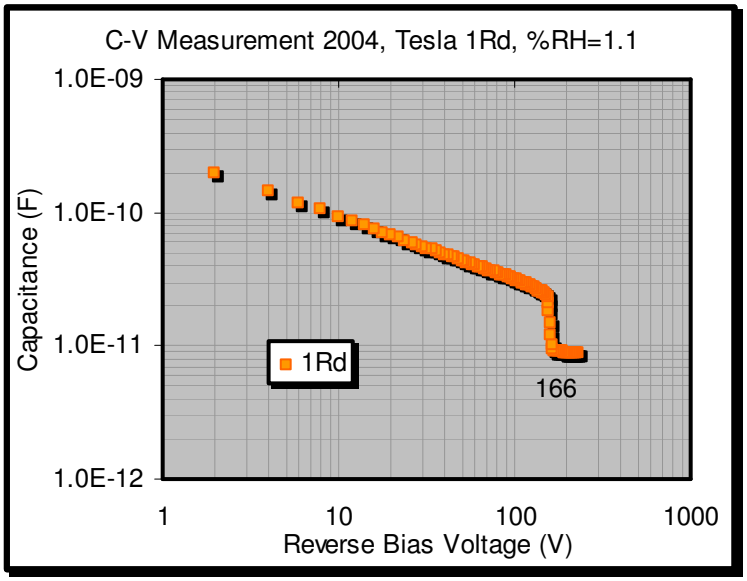

Chart 24: The measured depletion voltage was –166V.

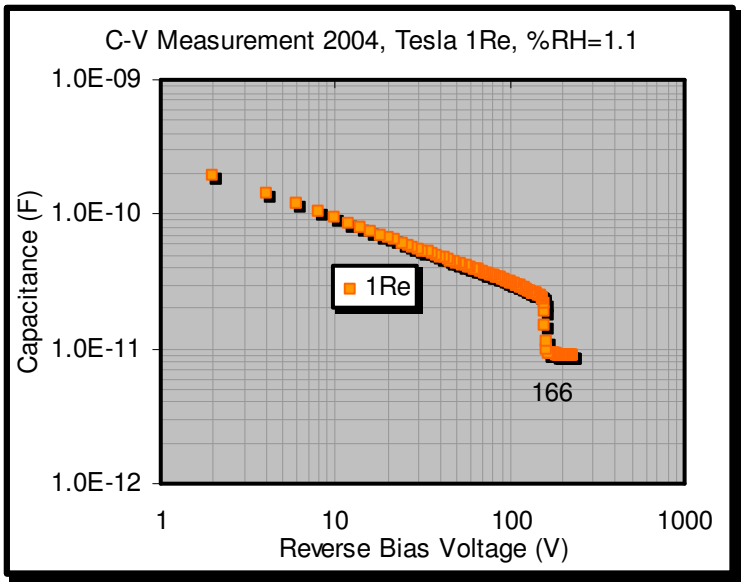

Chart 25: The measured depletion voltage was –166V.

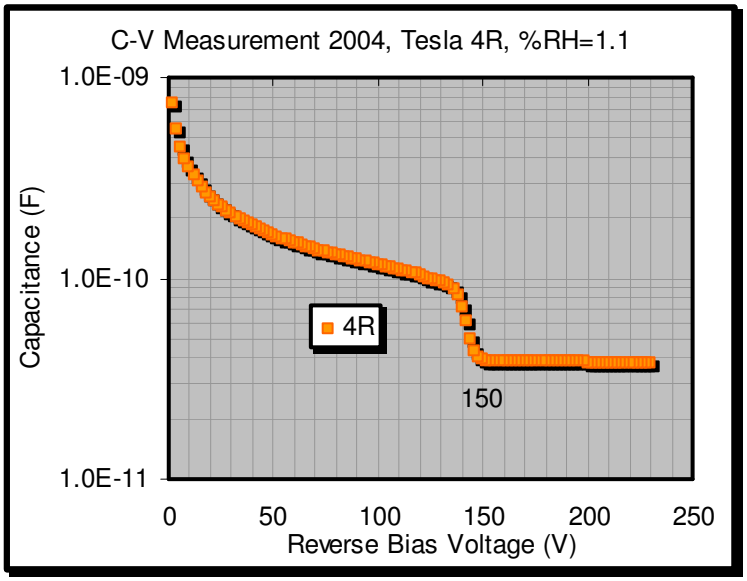

Chart 26: The measured depletion voltage was –150V.

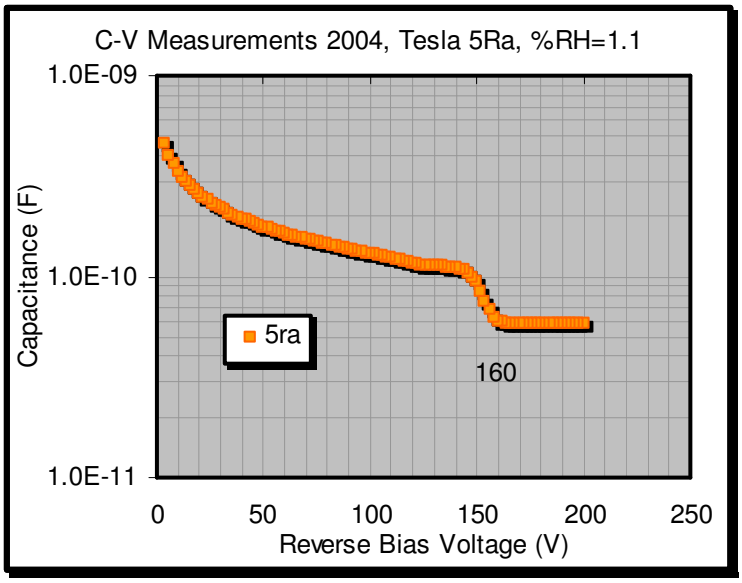

Chart 27: The measured depletion voltage was –160V.

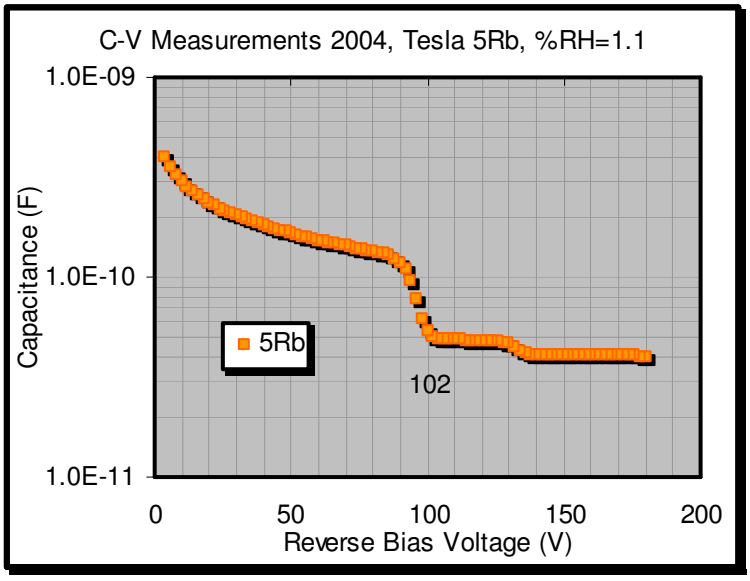

Chart 28: The measured depletion voltage was –102V.

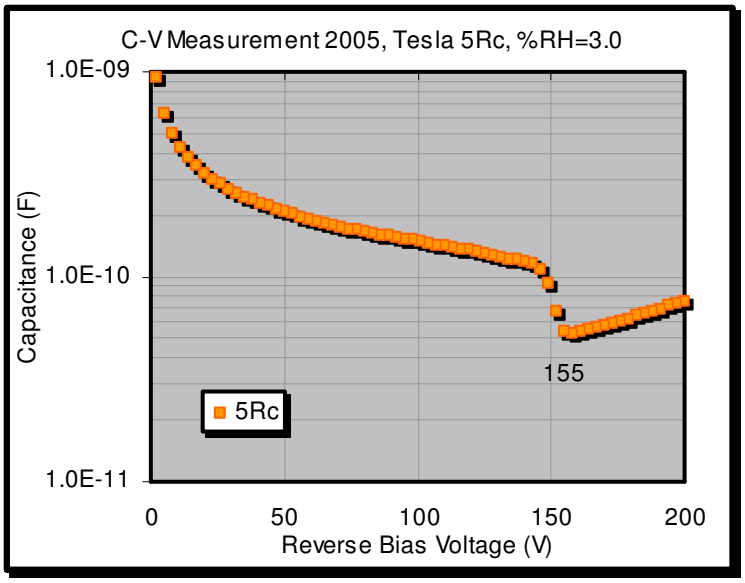

Chart 29: The measured depletion voltage was –155V.

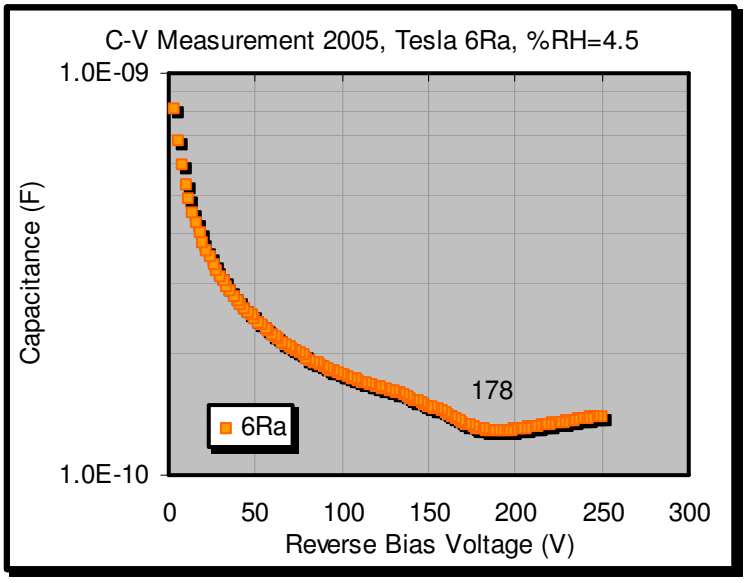

Chart 30: The measured depletion voltage was –178V.

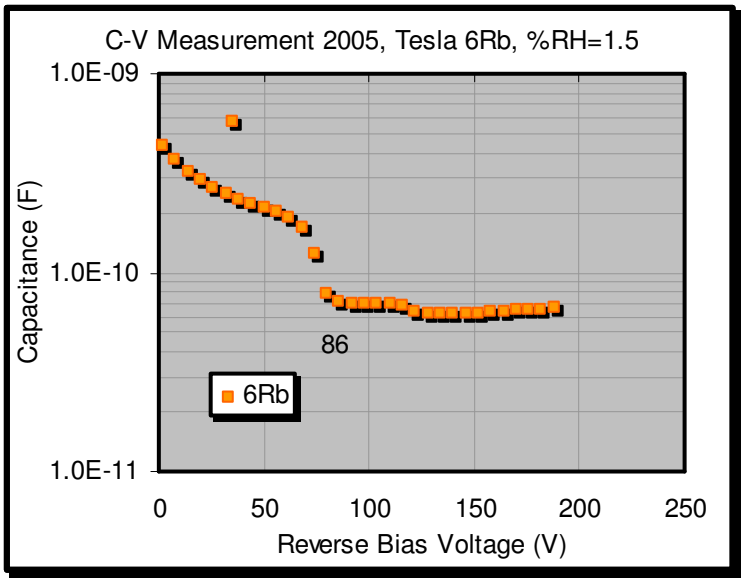

Chart 31: The measured depletion voltage was –86V.

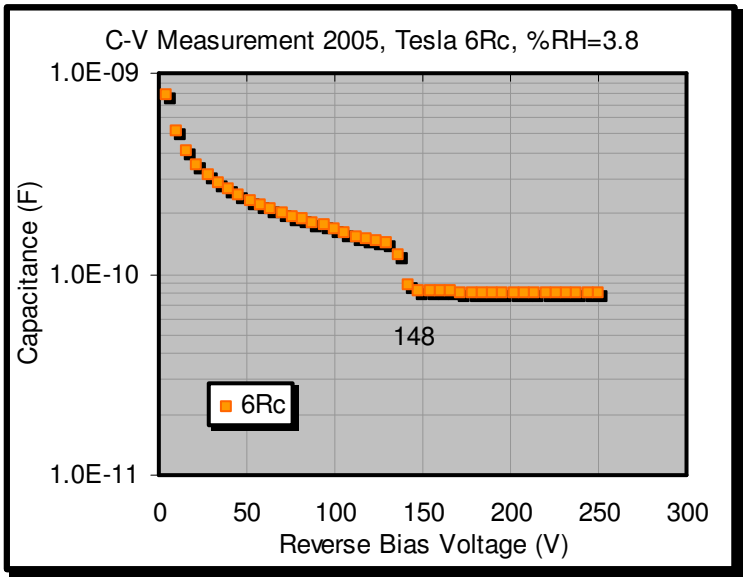

Chart 32: The measured depletion voltage was –148V.

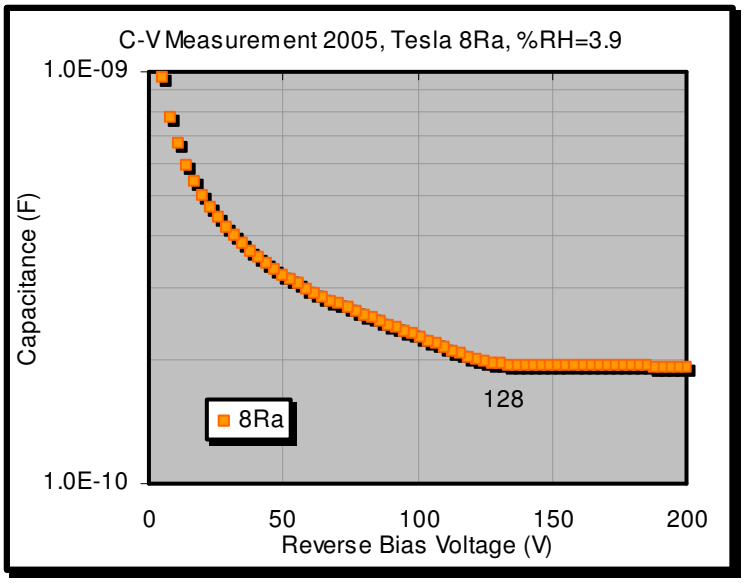

Chart 33: The measured depletion voltage was –128V.

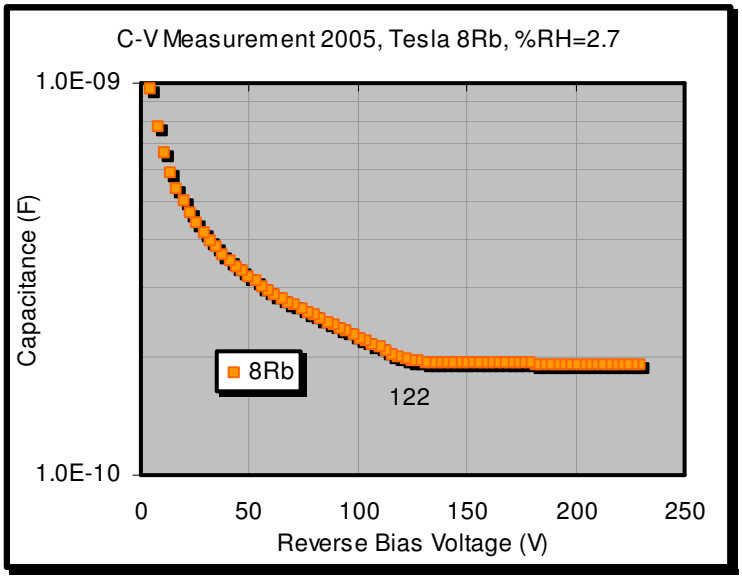

Chart 34: The measured depletion voltage was –122V.

A2. Quasi-3D Characterizations

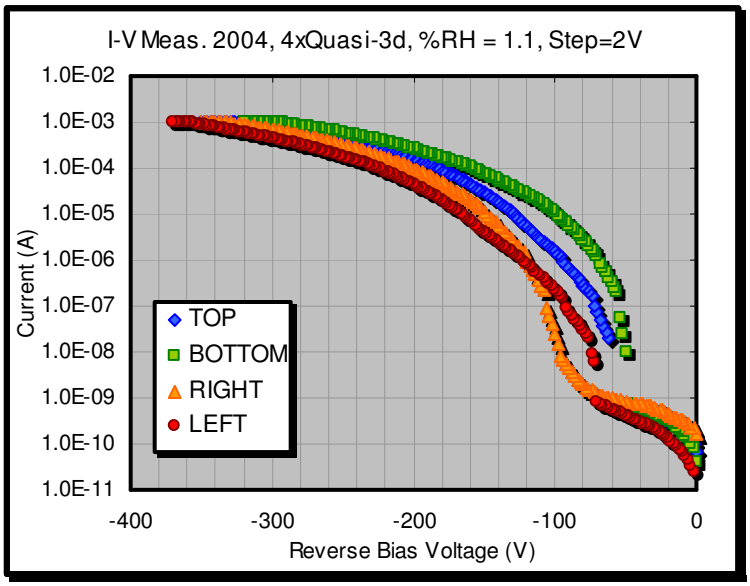

Chart 35: The smooth onset of avalanche breakdown seen here was due to the lateral current effects between the p+ spiral and the n+ spiral.

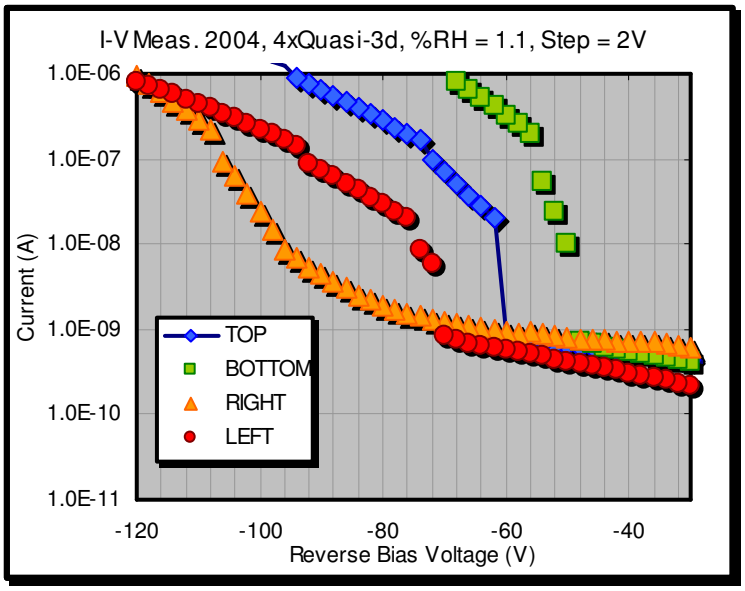

Chart 36: I made characterizations on four different quasi-3D structures that had punch-through effects at different voltages.

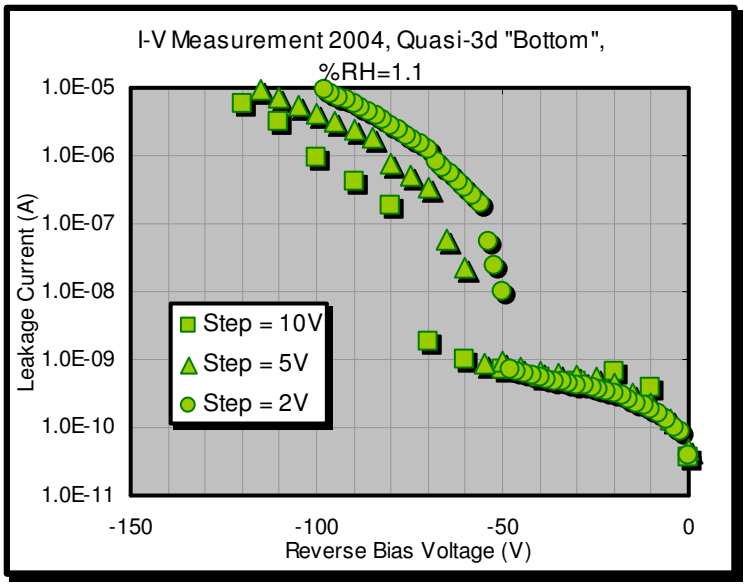

Chart 37: Due to the strong lateral current effects in the quasi-3D structures, different voltage step sizes affected the onset of the punch-through.

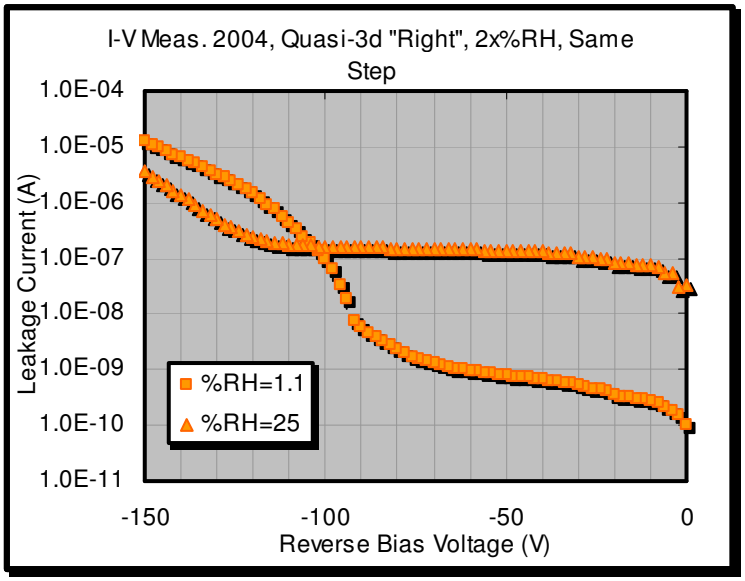

Chart 38: The small sizes of the quasi-3D devices were likely to be the cause for their strong humidity dependence.

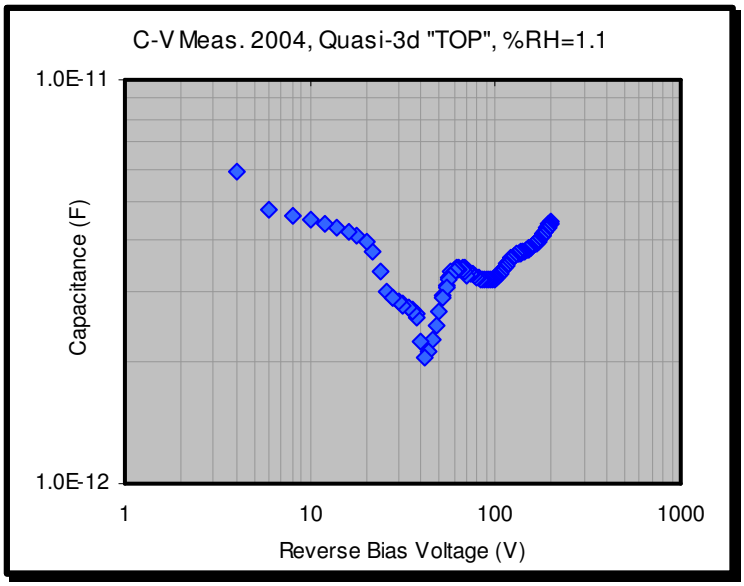

Chart 39: The strong lateral current effects in the quasi-3D structures, caused this C-V characteristic that was similar to the Tesla pixel detectors that also indicated lateral current effects.

A3. Analog Readout-Response

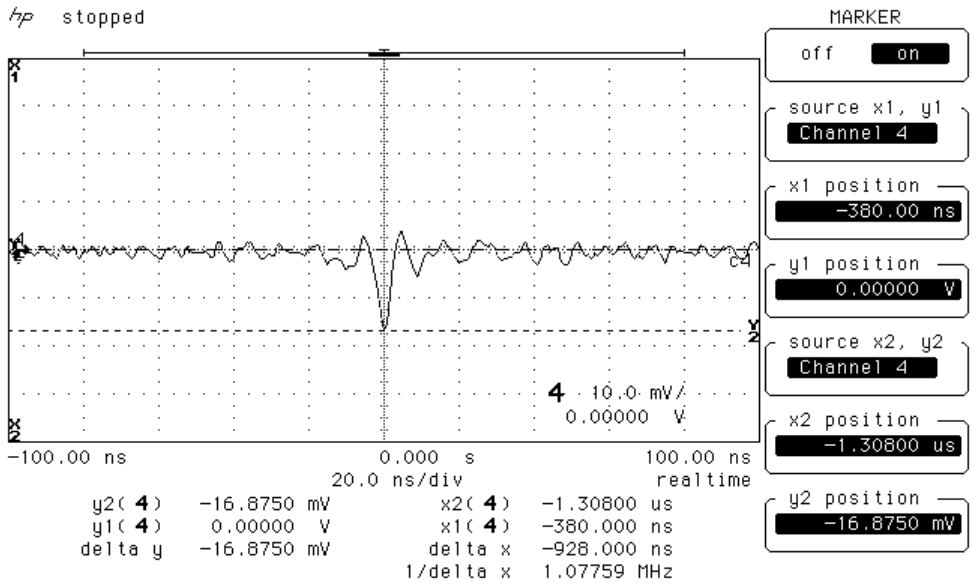

Figure 18: This snap shot shows a single photon event that was observed with the NA0068 MaPMT.

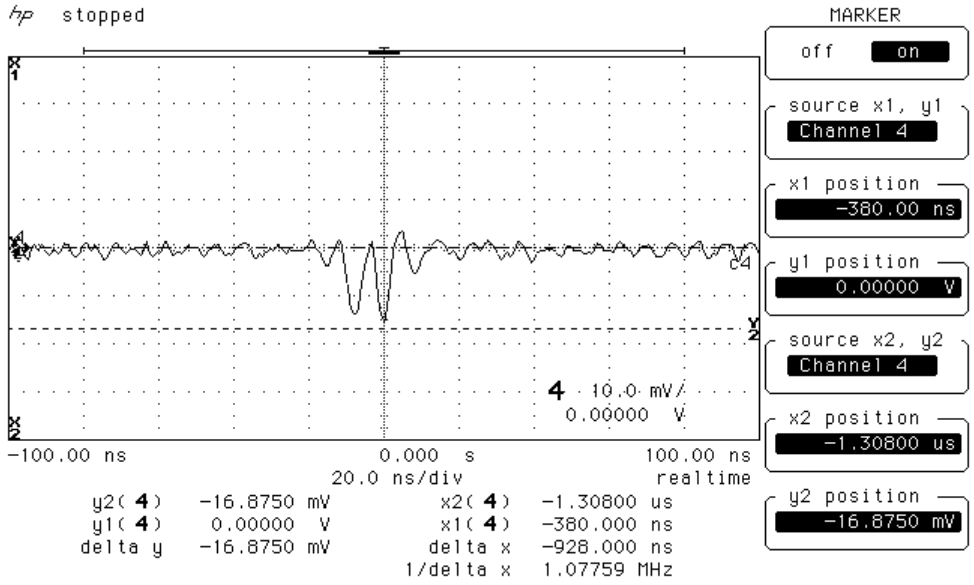

Figure 19: This snap shot shows a double photon event that was observed with the NA0068 MaPMT.

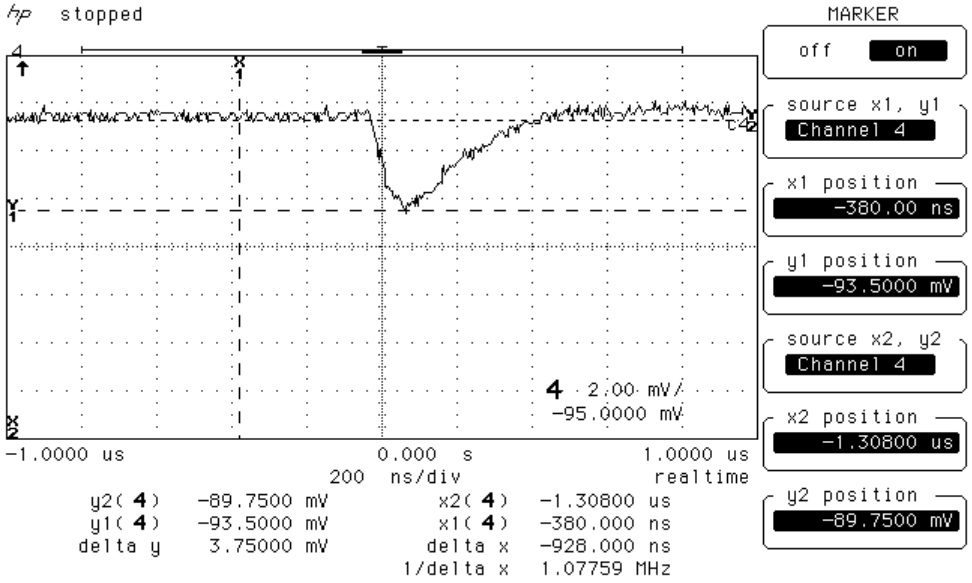

Figure 20: This is a snap shot of the analog ASIC output caused by a NA0043 MaPMT noise signal, under nominal configurations. This analog output had the characteristically small pulse height below 4mV.

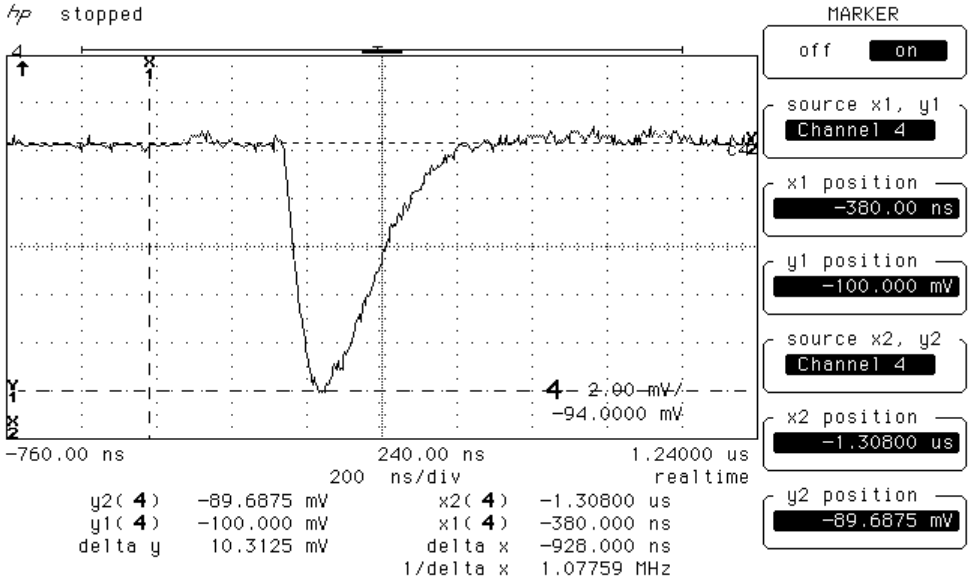

Figure 21: This is a snap shot of the analog ASIC output caused by a ZA1923 MaPMT single-photon induced signal, under nominal configurations. This analog output had a characteristic pulse height above ~4mV but below ~12mV.

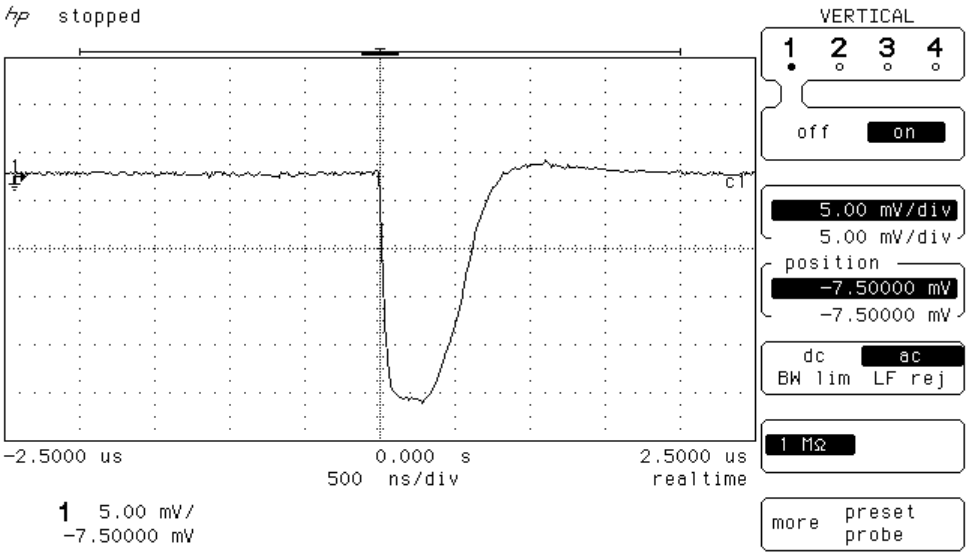

Figure 22: This is a snap shot of a saturated analog ASIC output caused by a NA0048 MaPMT signal, under nominal configurations. The MaPMT signal has in this case passed a too large amount of charge that the pre-amplifier could not handle, hence the flat "roof" on the signal that is due to charge conservation.

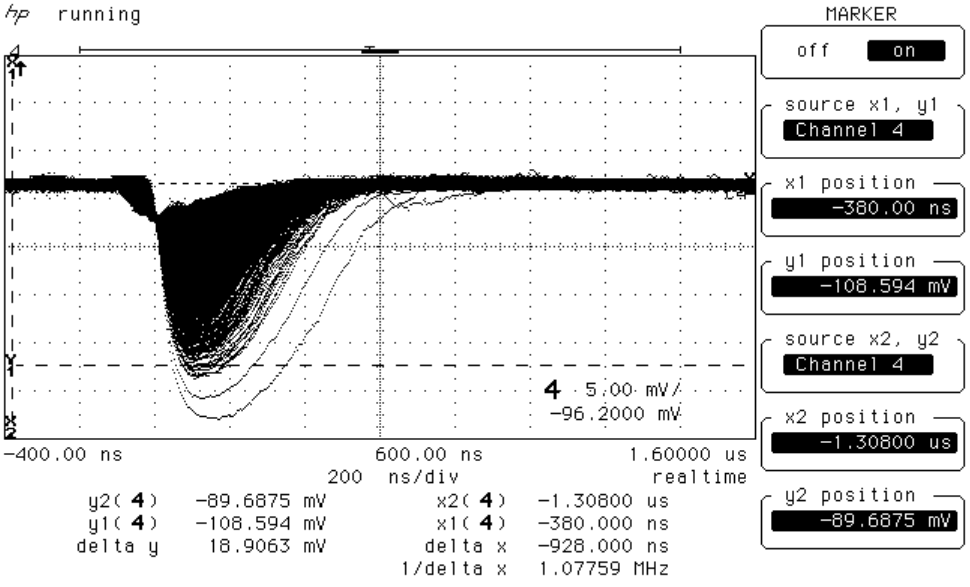

Figure 23: This is a snap shot depicts many analog ASIC output signals caused by a NA0048 MaPMT induced signals, under nominal configurations. We can only see few saturated signals, hence most of the signals are due to single-photon induced events.

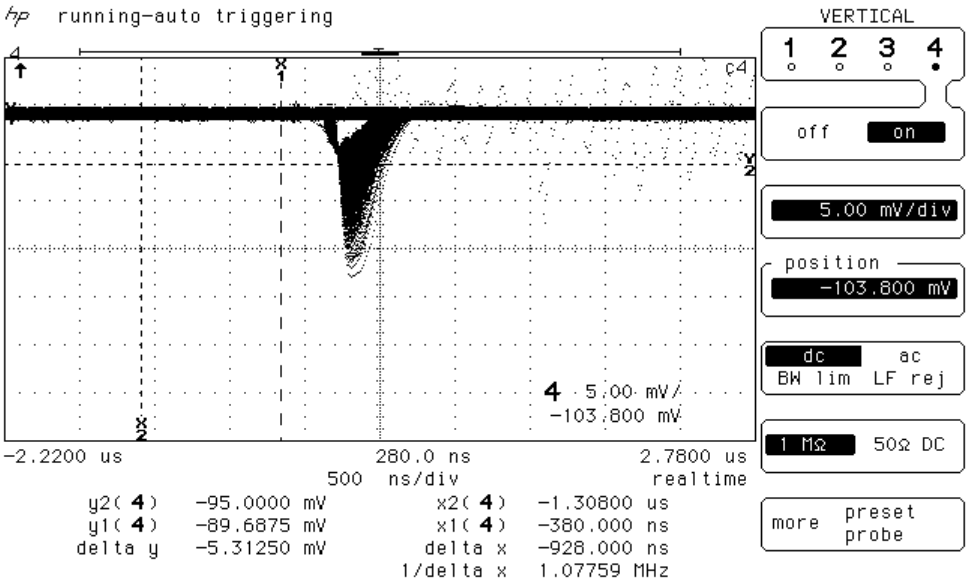

Figure 24: This is a snap shot depicts many analog ASIC output signals caused by a NA0068 MaPMT induced signals, under nominal configurations. We can only see few saturated signals, hence most of the signals are due to single-photon induced events.

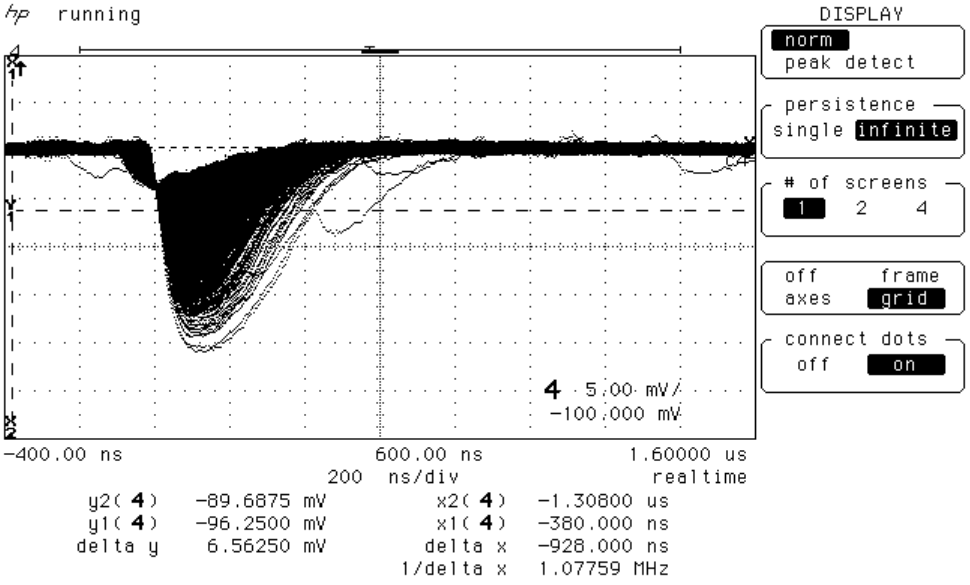

Figure 25: This is a snap shot depicts many analog ASIC output signals caused by a ZA1923 MaPMT induced signals, under nominal configurations. We can only see few saturated signals, hence most of the signals are due to single-photon induced events.

NA0048 pulse height distribution, HV1		
Pulse Generator	HV(V)	800
	PW (ns)	20
	PH(Vpp)	2.73
	Offset(V)	0
Oscilloscope	Trig Level (mV)	-3.3

Table 3: Measurement configurations for the low gain MaPMT.

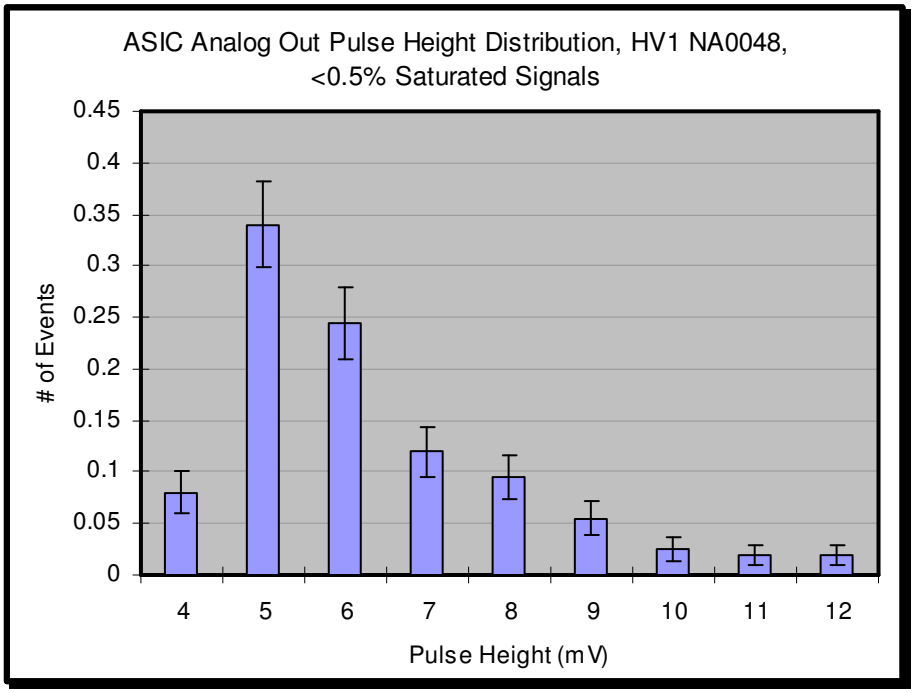

Chart 40: This pulse height distribution verifies that the dynamic range of the ASIC was properly matched with the low-gain MaPMT gain.

NA0068 pulse height distribution, HV2		
Pulse Generator	HV(V)	750
	PW (ns)	20
	PH(Vpp)	2.73
	Offset(V)	0
Oscilloscope	Trig Level (mV)	-3.3

Table 4: Measurement configurations for the medium gain MaPMT.

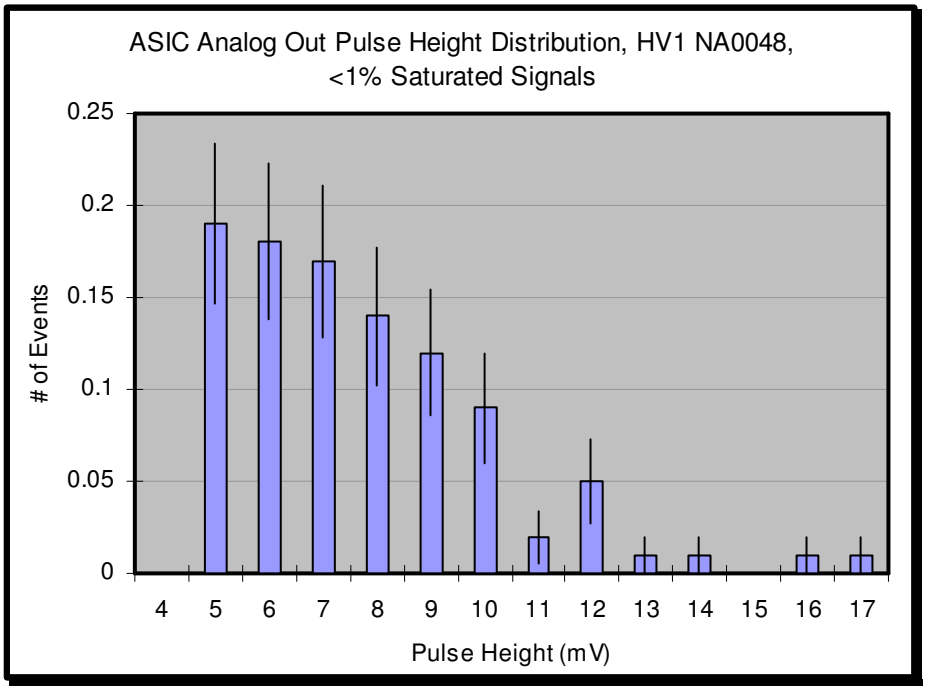

Chart 41: This pulse height distribution verifies that the dynamic range of the ASIC was properly matched with the medium-gain MaPMT gain.

ZA1923 pulse height distribution, HV3		
Pulse Generator	HV(V)	700
	PW (ns)	20
	PH(Vpp)	2.735
	Offset(V)	0
Oscilloscope	Trig Level (mV)	-3.3

Table 5: Measurement configurations for the high gain MaPMT.

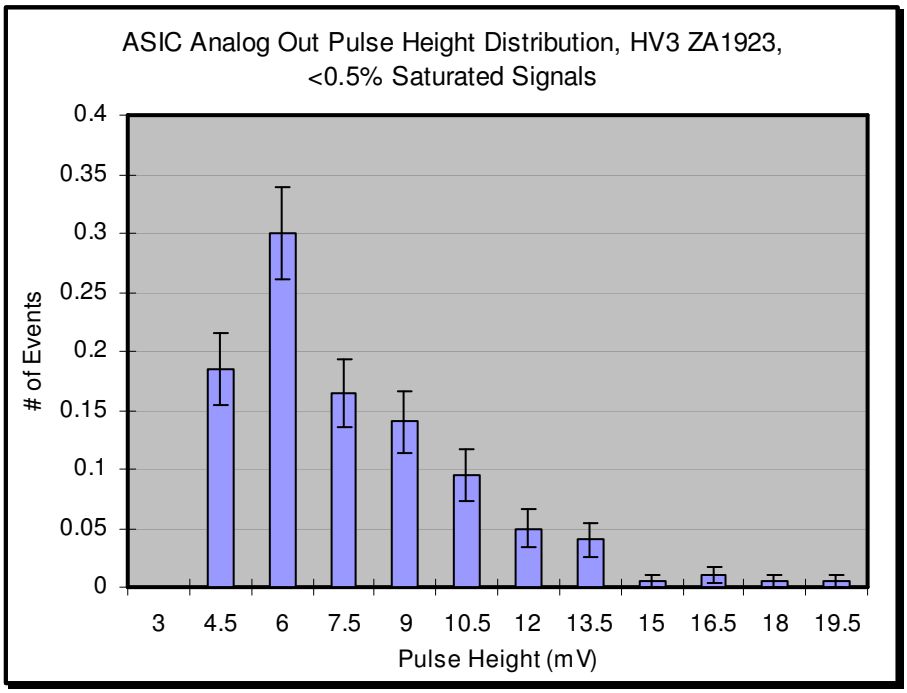

Chart 42: This pulse height distribution verifies that the dynamic range of the ASIC was properly matched with the high-gain MaPMT gain.